

**COSMIC RAY CAMERA DISCOSAT-1
CMOS CHARACTERIZATION USING A PROTON BEAM**

by CHRISTINA GAITANOU (cgai@itu.dk)

1 JULY 2024

MASTER THESIS : SOFTWARE DESIGN



Supervisors: JULIAN PRIEST & SEBASTIAN BÜTTRICH

STADS code: KISPECI1SE
IT UNIVERSITY OF COPENHAGEN

Acknowledgements

First and foremost, I am extremely grateful to my supervisors, Julian Priest and Sebastian Bütrich, for their continuous support, encouragement, assistance and guidance throughout the course of this project. It was truly a privilege and an inspiration to work among you and to be a part of the DASYA lab as a master's student.

My sincere thanks to the members of the DISCOSAT project, for offering me the opportunity to join their team and work on a real space application project.

I wish to thank the Physics Department of the University of Aarhus for providing their resources and facilities for the conducted experiments. In particular, I am deeply grateful to Anton Kristensen for his invaluable insights, help and enthusiasm.

I also extend my gratitude to the the Danish Centre for Particle Therapy at Aarhus University Hospital for their collaboration and for providing access to their research facilities for conducting the proton beam experiment. I would like to express my special thanks to Prof. Niels Bassler, for his assistance and guidance throughout the experiment.

This project would not have been be possible without each and every one of you.

Thank you.

ABSTRACT

This thesis explores the durability and performance of the Coral CMOS camera's use as a cosmic ray detector, as a part of the DISCOSAT-1 CubeSat's Image Processing Unit (IPU). The primary objective is to characterize the CMOS camera using a proton beam for energies that DISCOSAT-1 encounters in Low Earth Orbit (LEO) and further investigate the camera's capabilities in terms of dose measurement and energy dependency. In collaboration with Aarhus University, as part of the Danish Student CubeSat Program (DISCO), preliminary irradiation experiments were conducted using various radiation sources such as ^{238}U and ^{207}Bi . The main experiment involved exposing the camera to a proton pencil beam scanning (PBS) located in Aarhus University Hospital to collect a labelled dataset for characterization. Image processing techniques and statistical data analysis methods, including machine learning algorithms, were employed for feature extraction, data visualisation and interpretation. The irradiation experiments confirmed the camera's durability and efficiency as a particle detector and dosimeter without significant saturation. While the dose measurements were not precise, the proportionality was confirmed. The energy dependency did not yield to successful results, possibly due to insufficient data. The findings and challenges of this project aim to guide future camera characterization efforts within DISCO missions.

DISCARD THIS PAGE

TABLE OF CONTENTS

	Page
ABSTRACT	2
1 Introduction	5
2 Background	7
2.1 CubeSats	7
2.2 DISCOSAT-1	7
3 Methodology	9
3.1 Literature Review	9
3.2 Experimentation	9
3.3 Data Analysis	10
4 Literature Review	11
4.0.1 Cosmic Rays	11
4.0.2 Cosmic Ray Radiation	12
4.1 Radiation in Low Earth Orbit	13
4.1.1 SPENVIS	14
4.2 Complementary Metal-Oxide-Semiconductor (CMOS)	17
4.3 CMOS as a particle detector	19
4.4 Particle Classification	20
4.5 CMOS in nanosatellites	21
5 Experiments and Results	23
5.1 Irradiation experiments	23
5.1.1 ^{207}Bi	23
5.1.2 ^{238}U	24
5.1.3 ^{60}Co	24
5.1.4 ^{22}Na	25
5.1.5 Data acquisition	25
5.1.6 Data analysis	26
5.2 Proton beam experiment	36
5.2.1 Data acquisition	36
5.2.2 Data processing	40
5.2.3 Data analysis	44

	Page
5.2.3.1 Dose measurement	44
5.2.3.2 Energy	48
6 Discussion	52
6.1 Irradiation experiments	52
6.2 Proton beam experiment	54
6.2.1 Dose measurement	54
6.2.2 Energy	55
7 Future Work	57
7.0.1 Irradiation experiments	57
7.0.2 Proton beam experiment	58
8 Conclusion	59
LIST OF REFERENCES	103

Chapter 1

Introduction

The emergence of nanosatellites, particularly CubeSats, has democratized access to space, enabling a variety of organisations including universities, research institutions, and private companies, to participate in space missions. This accessibility is largely due to the standardization and miniaturization of satellite components, which simplifies the design and deployment process and reduces their cost. A key factor in their success and proliferation of CubeSats is the use of off-the-shelf (COTS) components such as CMOS (Complementary Metal-Oxide-Semiconductor) image sensors [1]. These commercially available components, originally developed for consumer electronics, are known for their high integration capability, low power consumption, high noise immunity and robustness in harsh environments. CMOS technology is widely used in a variety of applications today, including digital cameras, smartphones, automotive systems, medical imaging, and security cameras. While CMOS sensors are primarily used for imaging applications in satellites, their semiconductor material, compact size and low power requirements, makes them sensitive but also resilient to ionizing radiation, allowing them to detect and measure various forms of radiation [2].

The Danish Student CubeSat Program (DISCO) is a collaborative project between universities in Denmark that gives the opportunity to students to develop, design and operate a satellite. Their first 1U CubeSat, DISCOSAT-1, deployed in April 2023 with main mission to test and validate technologies for DISCOSAT-2 (3U CubeSat), and its now orbiting in Low Earth Orbit (LEO). The satellite is also equipped with a Tensor Processing Unit (TPU) chip and a CMOS camera sensor to operate as a Cosmic Ray Detector, instead of imaging. The Cosmic Ray experiment is designed to monitor the effects of radiation on the satellite's hardware components caused by ionization, which is essential for protecting onboard electronics from potential malfunctions and degradation. In previous research work, the software for particle detection was

developed and tested on a DISCOSAT-1 prototype, to measure the secondary cosmic ray flux at ground level. The radiation that DISCOSAT-1 is exposed to in LEO, includes high-energetic particles that are mostly protons. The deployment and testing of the software to validate the satellites Image Processing Unit (IPU) was not feasible, consequently, this thesis project aims to evaluate the CMOS camera's performance and reliability of the CMOS camera under irradiation conditions that represent the space environment through characterization.

Chapter 2

Background

2.1 CubeSats

CubeSats are a specific type of nanosatellites, built to standard dimensions of 10x10x10 cm and are categorized as 1U, 2U, 3U, or 6U in size [3]. Since their invention in 1999, they become a popular choice for both industry and academia due to their accessibility and relatively low cost. CubeSats have been deployed for various purposes, including studying Earth's atmosphere, space weather and biological sciences. Within technological missions, they have contributed in research fields such as space power, and radiation testing. CubeSats have revolutionized the space industry universally, by democratizing access to space and enabling a wide range of research and applications [4].

2.2 DISCOSAT-1

The Danish Student CubeSat Program (DISCO) is a collaboration initiative between Aarhus University, Aalborg University, University of South Denmark and IT University of Copenhagen. The program has launched its first satellite DISCOSAT-1 in April 2023 and preparing to deploy DISCOSAT-2 within 2025. DISCOSAT-1 is 1U CubeSat with a mass of less than 1.5kg and predicted design lifespan of 5 years. Ultimately, DISCOSAT-1 aims to demonstrate the viability of certain technologies for DISCOSAT-2 satellite: a larger 3U (10x10x30 cm) Earth-imaging satellite, equipped with two visible and one infrared camera that will assist in the climate research of Arctic Research Centre (ARC) by monitoring the region of Greenland. DISCOSAT-1 was successfully deployed in Low Earth Orbit (LEO) and there was an initial communication, but due to a lengthy ground station failure it was not acquired again. DISCOSAT-1's payload involved testing the image pipeline through a model system (IPU), which consists of a Tensor Processing Unit (TPU) chip within a Coral Board mini, and a Coral

camera. The camera's mission was to act as a particle detector aiming to investigate the impact of cosmic rays on the satellite's hardware components, particularly the camera and TPU. The camera's Complementary metal–oxide–semiconductor (CMOS) sensor, is well-suited for radiation detection due to its low power consumption, high sensitivity, and ability to integrate with other electronic systems. They have also proved to be more resistant to radiation-induced damage than many other technologies, making them suitable for extended space missions [5]. Cosmic ray detection in satellites is crucial for monitoring and mitigating the harmful effects of high-energy particles on electronic systems, ensuring the reliability and longevity of space missions.

In previous research project, the development of the camera control software was designed in Python, and tested on a prototype at ground level, for detecting cosmic ray events that reach the Earth. The detecting algorithm reads frames with a rate of 40 Frames Per Second (FPS), and processes them using the OpenCV library. Through greyscale conversion and thresholding contour extraction, the particle detections are isolated and recreated in a smaller size that makes them suitable for down-link. The camera resolution is set at 1920 x 1080 progressively displayed pixels (dpi). The script includes a logging set up for debugging and monitoring purposes and it can be found in the appendix under Cosmic Ray Detector .1.1. The threshold value was optimized through experimentation. Experiments included a simplified method for calculating the cosmic ray flux based on the data collected from these detection images [6]. The initial goal for the continuation of this thesis project was to deploy this cosmic ray detector script in the satellite, attempt to down-link the isolated particle detection images for analysis, and perform a particle count that would aid in monitoring the encountering radiation of the satellite orbiting in LEO. However, due to communication limitations, it was not possible to deploy and test the script on DISCOSAT-1. Consequently, the project's scope shifted to characterizing the performance of a commercial off-the-shelf (COTS) camera under radiation exposure. In collaboration with the Physics Department at Aarhus University, this study will explore the camera module's response to radiation particles, its survival, dose measurement, and energy dependency through irradiation experiments. Understanding the capabilities and limitations of a camera module in radiation environments is crucial for ensuring their reliability within satellite missions in LEO. This study will contribute in upcoming DISCO projects, concerning experimental setups and procedures in irradiation experiments that are necessary for testing and deploying radiation-sensitive technologies in space.

Chapter 3

Methodology

3.1 Literature Review

Literature review was conducted, in order to gain a comprehensive understanding of all the different elements that involve characterizing a CMOS sensor for cosmic ray radiation, as part of a nanosatellite's payload. This research starts with the importance of cosmic radiation and its effects on electronics, and continues with a thorough analysis of the radiation encountered in Low Earth Orbit (LEO), using the Space Environment Information System (SPENVIS) platform. Indubitably, it is essential to inquire CMOS sensor's imaging functionalities to develop a deeper understanding of how it operates as a radiation detector, with emphasis on DISCO-1 camera's architecture. Finally, similar works regarding the deployment of CMOS sensors in satellites in research, and the prospects of particle classification using images captured by CMOS sensors, are also discussed.

3.2 Experimentation

The characterization involves irradiation experiments, that will assess the camera's durability and performance as radiation detector. In collaboration with Aarhus University, the camera was initially exposed to various radiation sources and at a later stage, to a pencil proton beam located in the Aarhus University Hospital. The preliminary radiation experiments, took place in the Physics Department of Aarhus University, and they mainly act as tests to provide insights into the camera's behavior under radiation, and help to refine the experimental setup for the proton beam experiment. The proton beam experiment involves the camera irradiation using a proton pencil beam scanning (PBS), located in the Danish Centre for Particle Therapy at Aarhus University Hospital and described in 5.2. This experiment replicates the energy levels of cosmic radiation found in LEO more accurately than the initial tests. Therefore, the data acquired from this experiment provide a more direct assessment of the camera's resilience and

capabilities under conditions similar to those encountered by DISCOSAT-1. The duration of these experiments was short since they were conducted in a different city and with a limited access. Especially for the proton beam experiment, the approval process and booking of the appointment was delayed due to formalities. For that reason this project was also delayed and the proton beam experiment could not be repeated to increase the size of the dataset, or improve its measurements under a new set up. All experiments were scheduled and conducted through the collaborative DISCO project. Every section includes the experiment set up, data acquisition process and results.

3.3 Data Analysis

Data analysis is essential for interpreting the results from the experimentally acquired data. The collected data were categorised into classes according to their characteristics, defined by the conditions under which the experiments were conducted. More specifically, for the initial experiments, the characteristics concern the radiation source and the particle that each source plausibly emits. The characteristics for the data obtained from the proton beam experiment involve the dose and energy measurements as provided from the researchers. Image processing techniques were utilized to extract important features such as activated pixels and total intensity, aiding in determining the energy deposited in the sensor. Furthermore, by applying quantization and K-means clustering techniques, an algorithm was developed to segment and count particles, providing a detailed evaluation of the sensor's response to radiation. Statistical analysis of these features quantified dose measurements and assessed sensor performance. The data analysis also includes the development and utilization of machine learning techniques and algorithms such as Linear Regression Model for defining a linear relationship between variables, and Gaussian Mixed Models (GMM) used for unsupervised clustering.

Chapter 4

Literature Review

4.0.1 Cosmic Rays

Cosmic rays are high energy subatomic particles that travel at speeds nearing the speed of light causing ionization i.e. the production of ions by means of losing electrons [7]. These rays were first discovered by Victor Hess in 1912 during flights at high-altitude in hot air balloons when he observed that radiation levels increased with altitude. This suggested that these rays had extraterrestrial origin. Cosmic rays have been classified based on their origin and energy, with Primary Cosmic Rays (PCR) originating from outer space. Most of these are atomic nuclei, with approximately 89% being protons (hydrogen), 10% helium, and about 1% consisting of heavier elements [8]. When PCR enter the Earth's atmosphere, they collide with atmospheric nuclei, leading to ionization and the creation of Secondary Cosmic Rays (SCR). [9]. These secondary rays include mostly muons, pions, electrons, neutrinos, and γ rays, with muons being the predominant type that reaches the Earth's surface [10]. This phenomenon is also known as Extensive Air Showers (EAS).

PCRs are charged particles that accelerate along the magnetic field lines of the interstellar medium, up to the point that they acquire sufficient energy to escape. Their paths alter due to their charge across the magnetic field, and their precise origins render difficult to trace [11]. The source of PCRs has been a puzzle for physicists for a long time with various theories suggesting that they may come from the sun, beyond our solar system or even distant galaxies depending on their energy levels. In 2012, Luke O'C. Drury proposed that cosmic rays have three distinct aspects of origin: the particles themselves, their energy, their acceleration sites, but the particles with the highest energies are thought to be derived from supernova explosions [12]. However, conclusive evidence is still lacking.

Linear energy transfer (LET) as defined in dosimetry, is a measure of the amount of energy an ionizing particle deposits to the material when it passes through it, per unit of distance.

Essentially, this is a description of how radiation interacts with matter and it is a positive value by definition. Throughout this thesis project, the energy of particle refers to the radiation particle's LET energy value. Typically PCR s possess higher energies than SCR s, since they transfer part of their energy to their secondary produced particles. Their energy levels start at around 1 MeV, and most of these are classified as Galactic Cosmic Rays (GCR). They originate within the Milky Way but excluding PCR s that come from the Solar System. The highest energy cosmic rays (ranging from 10^{18} eV to 10^{20} eV - some reported above 10^{20} eV) are known as Ultra-high-energy cosmic rays (UHECR) and their origins are still unclear [13]. The Sun is a major source of low-energy cosmic rays on Earth, while high-energy cosmic rays mainly have a galactic origin. It is also important to stress that detection of UHECRs relies on observing the SCR s from Extensive Air Showers (EAS) [9].

4.0.2 Cosmic Ray Radiation

Research into cosmic radiation has been carried out both indirectly using ground-based equipment, and directly through devices placed in satellites. In the last decades significant advancements in space technology have been crucial in exploring the properties of cosmic radiation [14]. Firstly, it is paramount in protecting astronaut health since cosmic rays can cause significant radiation hazards, especially during long-duration missions. Continuous monitoring and precise detection permit the employment of effective protective measures to safeguard astronauts' health and safety. Secondly, comprehending the radiation environment via cosmic ray detection is critical in spacecraft design in order to build resilient to radiation. These high energetic particles can interfere and damage electronic systems within spacecrafts. They can cause single-event upsets (SEUs), latch-ups, and total ionizing dose (TID) effects, leading to data corruption, system malfunctions and permanent damage to electronic components [15]. SEU refers to disruption of the normal operation of electronic circuits by a single particle, potentially causing data corruption or even system failures, that are quite common. Total ionizing dose (TID) effects refer to prolonged exposure to radiation and they have the potential to degrade semiconductor materials which could lead to permanent damages [16]. For example, the recent solar storm in May 2024, one of the largest in over a decade, affected various spacecraft and instruments. The National Aeronautics and Space Administration's (NASA)Curiosity rover and the Mars Odyssey orbiter experienced disruptions. Curiosity's navigation cameras captured black-and-white streaks and specks caused by charged particles from the solar storm,

while the rover's Radiation Assessment Detector (RAD) recorded the highest radiation levels since its landing [17].

The study of cosmic rays enriches scientific knowledge, offering insights into their origins and the universe's processes relevant to their creation, which is vital for advancing the field of astrophysics [18]. Pierre Auger Observatory located in Argentina, is the largest setup in the world designed for observing ultra-high-energy cosmic rays. It uses a hybrid detection technique, consisting of water-Cherenkov detectors spread over 3000 square kilometers and fluorescence telescopes to measure the air showers that reach Earth [19]. Another example constitutes the Alpha Magnetic Spectrometer (AMS-02), which is a particle physics detector designed to study dark matter, antimatter, and missing matter from cosmic rays and it is mounted on the International Space Station (ISA). It is a very precise instrument concerning cosmic ray composition and flux measurements that provides crucial data on the nature and origin of cosmic rays [20].

The CREDO (Cosmic-Ray Extremely Distributed Observatory) project is a scientific initiative aimed to detect cosmic ray particles. It employs a wide network of detectors that are distributed globally, enabling a collaborative approach to cosmic ray research [21]. The project utilizes everyday devices such as smartphones and Raspberry Pi computers and turns them into cosmic ray detectors, leading in democratization of scientific research by general public participation[22]. DISCOSAT- 1's payload was inspired by the CREDO project and was equipped with a CMOS camera in its IPU aiming to observe the cosmic ray impact on the TPU and camera components. This thesis project is mostly concerned with high-energetic protons as DISCOSAT-1 will encounter in LEO.

4.1 Radiation in Low Earth Orbit

Radiation exposure analysis encountered by DISCOSAT-1 in Low Earth Orbit (LEO) is a significant factor for the camera's characterization under the specific space environment. Understanding the radiation that the camera will be exposed to is vital for ensuring the camera sensor's reliability and overall performance during its mission. The space environment in LEO consists of three main sources of radiation: GCRs, trapped particles, and solar particle events (SPE) [23]. All these radiation particles are strongly affected by the Earth's magnetic field [24]. Some advanced satellite missions dedicated to radiation detection and monitoring are described below, highlighting the importance of ionizing radiation in the space environment.

The PAMELA (Payload for Antimatter Matter Exploration and Light-nuclei Astrophysics) and SATRAM (Space Application of Timepix based Radiation Monitor) are two well known missions involved in studying the radiation environment. PAMELA is a satellite-based experiment developed by the Italian Space Agency (ASI) that was launched on June 15, 2006 and is designed to study high-energy protons and antiparticles such as positrons and antiprotons [25]. The data collected by PAMELA have proven valuable since they provided insights into the trapped particle radiation in the inner Van Allen belt and have contributed in the accuracy improvement of radiation models [25]. These findings showed that the fluxes exhibit a declining trend with increasing energies [25]. SATRAM which was launched on May 7, 2013 aboard the European Space Agency's (ESA) Proba-V satellite, is a radiation monitor developed by the Czech Technical University in Prague in collaboration with ESA. This instrument is dedicated to monitor and record the radiation environment in LEO using the Timepix hybrid semiconductor pixel detector [26]. This detector provides single particle counting, tracking and energy loss measurements for ionizing radiation. SATRAM continuously samples the mixed radiation field along the satellite orbit, providing important data on dose rates, equivalent dose rates, and particle-type count rates[24].

The intensity of GCR fluxes at different altitudes has been analyzed and compared in order to determine their significance in the Earth's orbit by means of spatial analysis of these particles in LEO and near equator orbit (NEqO). The aim has been to compare GCR fluxes with the intensities of SEPs and trapped particles in the radiation belt [23]. Utilizing the Razaksat satellite orbit data to analyze GCR fluxes at different altitudes, the results indicated that the fluxes decrease with increasing energies but increase with respect to altitudes. The study also showed that GCR dominated the higher energy range of about 10 GeV and above, while trapped particles dominated the lower energy range of a few tens of MeV [23].

4.1.1 SPENVIS

DISCOSAT-1 is orbiting at 550km altitude. By utilizing the Space Environment Information System (SPENVIS) platform, the radiation that will encounter can be simulated with different predicting models. SPENVIS is an online platform developed by ESA that offers tools for analyzing the space environment's effects on spacecraft, including radiation and meteoroid impacts [27]. To understand the potential radiation impacts on DISCOSAT-1 camera, the data provided by the satellite's Two-Line Element (TLE) set were used as input in the SPENVIS

platform. This allowed the prediction modelling for the trapped protons and GCR fluxes as DISCOSAT-1 is orbiting. SPENVIS offers multiple models and different plots for solar maximum and minimum activity for a detailed environmental analysis and prediction. This project's research is mainly focus on proton fluxes and energy levels.

We are now in a period of increasing solar activity as we move towards the peak of Solar Cycle 25. This cycle began in December 2019, and the solar maximum is now expected to occur between late 2024 and early 2026, with some predictions suggesting a peak as within 2024 [28]. During solar maximum, the Sun exhibits higher levels of activity, including more frequent and intense solar flares and coronal mass ejections (CMEs) [29]. The plot figures in 4.1, are models for predicting the radiation proton flux that DISCOSAT-1 encounters in LEO, using the SPENVIS platform. The first figure 4.1a shows the ion spectrum of GCRs by visualising the integral and differential fluxes (dotted and solid lines respectively) versus the energy of the proton particle, which is ranging from 10^0MeV/n to 10^5MeV/n . The integral flux presents the cumulative number of particles, whereas the differential concerns the number of particles per unit energy interval. This analysis will focus on the values of energy ranged that of the proton beam experiment described later in 5.2, which is about 5 - 250 MeV. The integral flux at 5 MeV is approximately $10^3 \mu^{-2} s^{-1} sr^{-1}$ and at 250 MeV drops to $10 \mu^{-2} s^{-1} sr^{-1}$, suggesting that DISCOSAT-1 will frequently encounter low-energy GCR protons but the high-energy ones will be much less frequent. Typical for GCRs, the differential flux (rate of particles at each energy) decreases rapidly as energy increased. The second plot in figure 4.1b is a similar visualisation for the solar protons total flux representing the overall long-term exposure of these radiation particles in LEO using the ESP-PSYCHIC model, followed by the figure 4.1c that shows a worst-case scenario for short-term periods under solar maximum, using the CREME-96 model. The integral fluence at 5 MeV is approximately $10^{11} cm^{-2}$ and it drops to around $10^8 cm^{-2}$ at 250 MeV. Similarly to GCRs, the differential flux also decreases as energy increases, indicating fewer high-energy protons. As expected, the first plot has higher differential fluence values at lower energies, whereas the second has lower differential values reflecting a high-impact period.

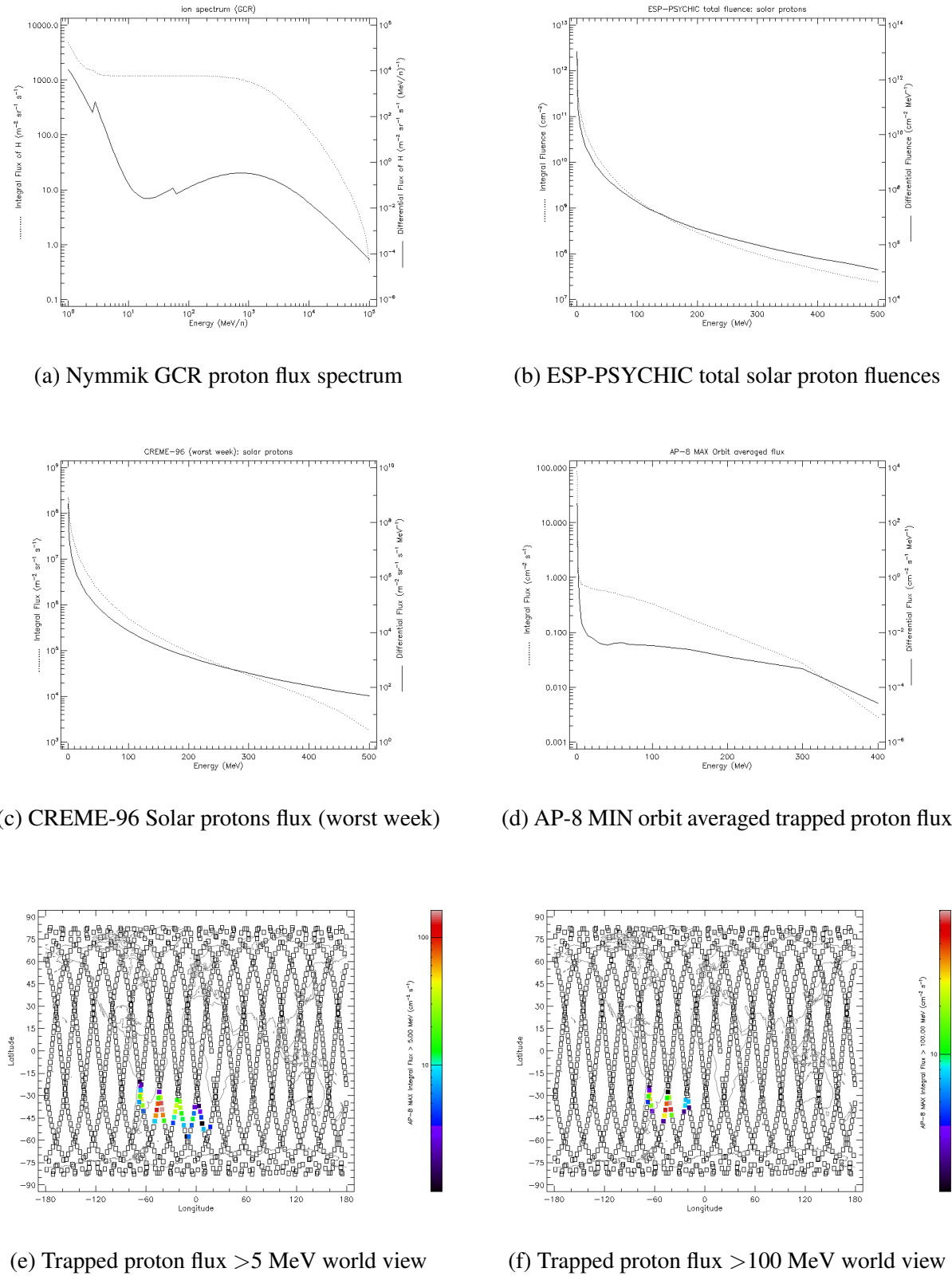


Figure 4.1: SPENVIS analysis plots for DISCOSAT-1

The last three plots of this figure 4.1d, 4.1e, 4.1f show the average trapped proton fluxes and the geographical distribution plots of the integral flux with energies >5 and >100 respectively,

which highlight the region with significant fluxes around the South Atlantic Anomaly. The integral flux of the average protons decreases significantly, indicating a higher frequency of encounters with lower-energy protons. Protons with energies above 100 MeV are less frequent but still notable in high-flux regions, and the differential flux shows a continuous decrease with increasing energy. The geographical distributions across DISCOSAT-1's orbit implies more frequent encounters with trapped protons in the 50-100 MeV range compared to those greater than 100 MeV. The overall analysis of these graphs indicates that protons with energies between 5 and 100 MeV are the most frequently encountered, particularly in the regions influenced by the Earth's magnetic field. Although high-energy protons (>100 MeV) are less frequent, their presence in specific high-flux regions and during peak solar events are still encountered.

4.2 Complementary Metal-Oxide-Semiconductor (CMOS)

As commercial off-the-shelf (COTS) components, which means they are readily available and affordable and easy to integrate, CMOS sensors consume low power, with high spatial resolution that ensures detailed imaging. By providing real-time data, it allows for continuous monitoring and immediate adjustments during experiments with precise measurements. They can also be calibrated for specific parameters, enhancing the accuracy and reliability of scientific data. For all these reasons, they have been used widely in scientific applications, and they have shown better sensitivity and a lower cost in comparison to the traditional Charge-Couple Device (CCD) sensors [30], [31].

A CMOS sensor is a semiconductor device that converts light into electrical signals. It is composed of millions of photodiodes, each representing a pixel. When light strikes these photodiodes, it generates an electrical charge proportional to the intensity of the light. These charges are then read and converted into digital values. Each photodiode in a CMOS sensor has an amplifier located nearby. These amplifiers convert the electrical charges into voltages. This proximity allows for faster readout and processing, reducing noise and improving image quality. The voltages are then converted into digital signals by on-chip Analog-to-Digital Conversion (ADC). This conversion turns the continuous voltage values into discrete digital values, which represent the brightness levels of each pixel. The digital signals are processed by the camera's (Image Signal Processor (ISP)). This stage includes various enhancements such as noise reduction, white balance adjustment, color correction, and compression. Last but not least, the Interface handles the transmission of processed image data from the ISP to external

devices or storage to ensure the data is correctly formatted and transmitted. The figure 4.2 depicts the functional workflow of a CMOS camera system, as described above.

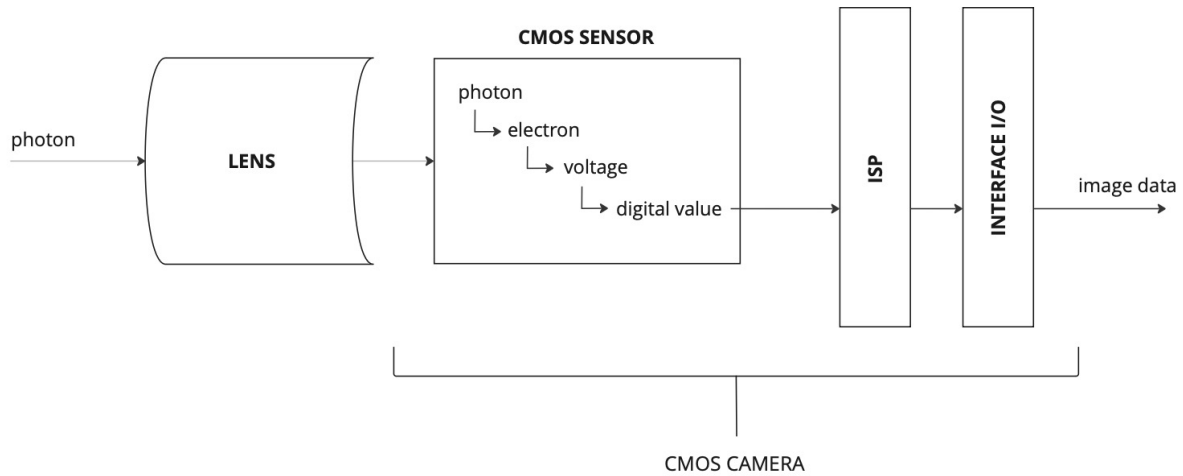


Figure 4.2: Example schematic diagram of a CMOS camera's components.

The Coral camera that is a part of the IPU of the DISCOSAT-1 satellite, consists of the OmniVision OV5645 CMOS sensor. This is a high-performance 5-megapixel sensor, with an active array size of 2592 x 1944 pixels that utilizes Back-Side Illumination (BSI) technology. BSI CMOS sensor is a type of image sensor designed to enhance light sensitivity and image quality. Unlike traditional front-side illuminated (FSI) sensors, BSI sensors have their photodiodes positioned closer to the light source by relocating the metal wiring to the back. The figure 4.3 illustrates a BSI CMOS sensor, where light passes through microlenses and color filters before reaching the photodiodes. These photodiodes convert light into electrical charges, with metal wiring positioned behind them. This design improves light absorption and reduces interference, resulting in better performance in low-light conditions [32]. The Coral camera is transmitting the processed data via the high-speed MIPI CSI-2 (camera serial) interface [33].

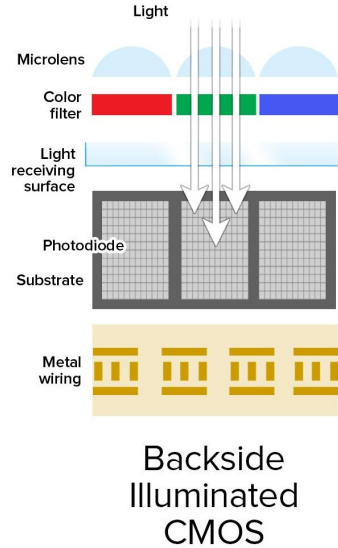


Figure 4.3: BSI CMOS architecture (Credit: Bob Al-Greene).[32]

4.3 CMOS as a particle detector

CMOS semiconductor cameras, are widely used in consumer electronic devices such as smartphones, webcams and digital cameras. Repurposing these cameras as radiation detectors leverages existing technology and reduces the need for specialized, often expensive radiation detection equipment. These cameras offer high spatial resolution, permitting detailed imaging of radiation particles. This is particularly beneficial in fields requiring precise localization of radiation, such as medical imaging and materials science. There are various works on radiation detection using CMOS sensors including alpha and beta particles, X-rays and gamma rays [30], [34].

Alpha (α) particles consist of two protons and two neutrons bound together into a particle identical to a helium nucleus. They are relatively large and carry a double positive charge and due to their size and charge, they are considered to have a low penetration power which means that they can be stopped by a sheet of paper or the outer layer of human skin [35].

Beta (β) radiation can either be β^- or β^+ . Beta minus radiation comprised of electrons ejected from the nucleus when a neutron breaks down into a proton, an electron, and an anti-electron neutrino. Beta plus radiation on the other hand, involves the emission of positrons, the antimatter counterparts of electrons. These are produced when a proton in the nucleus decays into a neutron, a positron and an electron neutrino. β particles being lighter than alpha particles and carrying a single charge, they can penetrate further. Materials like aluminum foil are

required to be stopped [36].

X-rays are a type of electromagnetic radiation with wavelengths ranging from 0.01 to 10 nanometers. They are highly energetic and can penetrate most materials at a varying degree. X-rays consist of high-energy photons rather than particles, in contrast to α and β particles. This property enables them to penetrate through soft tissues and produce detailed images of bones and internal organs, thus making them suitable for extensive use in medical imaging. Prolonged exposure to X-rays however, has the potential to damage electronic components which may also result in malfunctions[37].

Gamma (γ) rays are not particles with mass like α and β particles. They are high-energetic photons, emitted by the nucleus during radioactive decay when it descends from a high energy state to a lower one. Furthermore, γ rays have no charge and are extremely penetrating, with the ability of going through several centimeters of lead. Their ability to ionize molecules inside living cells, potentially causing damage renders them a health hazard [38].

The sensor detects radiation by measuring the ionization charge produced when ionizing particles interact with the pixels of the sensor. When ionizing particles such as α particles, β particles or γ photons pass through the sensor, they create ionization charge through the photoelectric effect or other mechanisms. This ionization charge is then collected and measured by the sensor. The amount of charge collected is proportional to the energy deposited by the particle, and this information can be used to determine the type and energy of the particle [31]. Literature review suggests that the sensor can be calibrated to distinguish different types of particles based on the amount of charge collected and other characteristics of the events, such as the spot size or maximum pixel value. [39]. Obtaining the dose rate from radiation detection images is also feasible[40], [41]. By analyzing the patterns and characteristics of the events recorded by the sensor, it is possible to classify the particles and differentiate them from other sources of radiation.

4.4 Particle Classification

Particle classification with CMOS image sensors involves analyzing the sensor's response from different particles and comparing the charge and pattern recorded. By analyzing the quantities of charge produced by the particles and the size of the spot mark on the sensor, an algorithm is developed which performs the classification. Methodologies employed include

placing specific threshold values for charge, radius and pixel to identify the type of particle. This method is employed in ionizing particles' detection and classification in several fields such as medical imaging, radioprotection and environmental monitoring [39]. CMOS sensor's ability to convert particle interactions into digital signals with high accuracy and low noise enhances its functionality as a radiation detector. An energetic particle, while it passes through the sensor, deposits a quantity of energy (ionizing particles affect multiple pixels in the CMOS imager) releasing charge which is captured in the sensitive epitaxial layer (part of the Substrate layer depicted in 4.3) [42].

In recent years the use of machine learning for classification purposes, such as identification of particle composition in cosmic rays has become popular. Machine learning algorithms have the unique ability to process large amounts of data, produce and implement patterns and relationships for precise predictions and classifications. In the case of particle composition classification, machine learning models are trained on a dataset that includes various features such as energy, angle of arrival, and number of muons or electromagnetic particles in the cascade [43] . These models learn from the data and then classify new instances based on these learned patterns. This approach has made possible an automated classification process and the production of precise and efficient results compared to traditional methodologies [44], [45] .

It's important to mention that these models are using raw data that provide high accuracy. Many variables such as exposure, gain, white balance are thoroughly considered and fine-tuned. This is not feasible for DISCOSAT-1's camera and it is considered a limitation. Furthermore, these experiments are conducted under very detailed set ups in very controlled environments, with high accuracy equipment for verifying the results obtained. However, theory suggests that the DISCOSAT-1 camera is still able to detect radiation particles, but in a more simplified way due to our limitations and restrictions. It's accuracy and capability in terms of particle classification and particle energy dependency deposited, is to be discovered through this research work. Additionally, there is limited research on predicting particle energies from proton detections using CMOS image sensors. The main focus has been on studying SEUs in CMOS caused by proton irradiation [46], but not on energy prediction.

4.5 CMOS in nanosatellites

CMOS imaging sensors, have become increasingly popular for use in space missions, particularly in nanosatellites. They are often used in remote sensing instruments to capture images

with high spatial resolution. However, they present some vulnerability to radiation effects that degrade the performance of the sensors and lead to functional interruptions or even destruction of components as mentioned in section 4.0.2. These COTS sensors offer high signal-to-noise ratios, integrated readout electronics, and low-cost procurement. They are often used in remote sensing instruments to capture images with high spatial resolution. These sensors, enhanced by software, can also detect ionizing particles, improving the fault tolerance of imaging instruments without extra hardware.

A challenge in using COTS CMOS sensors in space missions, is their vulnerability to radiation effects, such as displacement damage (DD) that can occur in semiconductor materials. This effect cause the formation of defects that increase dark current, noise, and leakage current, ultimately degrading the performance and reliability of electronic device. Additionally, critical parameters like the epitaxial layer thickness are often unknown but by using a simplified calibration method for characterization, this thickness and calibrate energy sensitivity can be calibrated with minimal effort [42]. It has been shown that the energy deposited by ionizing particles is linked to the intensity of the resulting clusters and this method is used to assess the energy sensitivity of CMOS imagers for detecting such particles on nanosatellites. These findings suggest that commercial CMOS sensors can be effectively employed as radiation monitors in these small satellites.

Consequently incorporating CMOS technology in nanosatellites for radiation detection purposes has been utilized in space missions, and it is considered a robust and efficient solution. An application of such use constitutes the employment of CMOS imaging sensors in nanosatellites that detect ionizing particles. This approach segments radiation-induced image artifacts, enhancing fault tolerance and measuring radiation environments, which aids in extending the satellite's operational life [47]. Another application is the one on Lucky 7 1U CubeSat, which employs a scintillator detector and CMOS-based PIN diode to examine and research cosmic radiation [48].

Chapter 5

Experiments and Results

5.1 Irradiation experiments

As a preparation for the main experiment and an initial test of the camera's use as a particle detector, we conducted irradiation experiments using different radiation sources in collaboration with the Physics Department of Aarhus University. As mentioned in 4.4, there have been various successful works on particle classification in the past using a CMOS sensor, but these were under very controlled and precise environments, utilizing raw data and the gain and exposure settings. In this experimental set up, the type of the detected particles can not be confirmed by any instrument, and it is instead based on the theory of radioactive decay and each source's decay equation. Nevertheless, these experiments aim to examine the sensitivity of the DISCOSAT-1's camera under irradiation, and show the prospects of classification and differentiation between particles. The software used for particle detection was developed in a previous research project and it can be found in the appendix under Cosmic Ray Detector .1.1. The radiation sources were chosen to investigate alpha (α), beta (β) and gamma (γ) particle detections with a few iterations to increase the amount of data gathered for analysis. It is important to notice that this camera driver does not support the control of exposure, gain or white balance, and thus these parameters function automatically.

5.1.1 ^{207}Bi

Bismuth-207 (^{207}Bi) is a radioactive isotope of bismuth with a half-life period of approximately 32.9 years. The decay primarily occurs by electron capture (EC), leading to the following decay equation:



In this equation the parent nucleus is ^{207}Bi , and the daughter nucleus is ^{207}Pb . The emitted β particle (or electron) is represented by β^- and the antineutrino that is emitted through the decay process is denoted by $\bar{\nu}_e$ [49]. The decay spectrum of ^{207}Bi includes β particles with a maximum energy of 806.5 keV and an average energy of 383.4 keV, internal conversion electrons with energies ranging from 481.7 to 1061 keV and γ rays with energies from 328.11 to 1770.2 keV. Additionally, the source emits X-rays with energies of 9.18-15.8 keV and 74.2 keV, and Auger electrons with energies of 5.2-15.7 keV and 56.0-88.0 keV respectively [50] [51].

5.1.2 ^{238}U

Uranium-238 (^{238}U) is the predominant isotope of uranium, since it accounts for 99% of the uranium found naturally. This radioactive isotope undergoes α decay that involves the release of a helium-4 nucleus from its parent atom, but it also emits various types of ionizing radiation across its half-life of approximately 4.47 billion years [52] [53]. Uranium-238 transitions through various stages throughout its complex decay chain, before it eventually becomes Lead-206 [54]. The equation of the α decay stage is:



where, $^{234}_{90}\text{Th}$ denotes the Thorium-234 isotope, as the product of the decay, and ^4_2He represents the α particle released during the decay, with energy around 4187 KeV [55].

5.1.3 ^{60}Co

Cobalt-60 is a synthetic radioactive isotope of cobalt that undergoes β minus (β^-) decay with a half-life of 5.27 years and equation:



where, $^{60}_{28}\text{Ni}$ represents Nickel-60, e^- is the β particle (electron) and $\bar{\nu}_e$ denotes the anti-neutrino emitted during the decay [56]. The newly formed Nickel-60 nucleus is initially in an excited state. In order to reach its ground state, it releases energy by emitting two γ rays with energies 1.17 MeV and 1.33 MeV [53]. This isotope is highly radioactive but it is used in many applications such as cancer treatment, industrial radiography and food irradiation since it can kill bacteria under controlled environments[57].

5.1.4 ^{22}Na

The radioactive isotope Sodium-22 (^{22}Na) is artificially produced and undertakes β plus (β^+) decay with half-life of approximately 2.602 years. In this process, a neutron in the sodium-22 nucleus is converted into a proton, an electron and an antineutrino. The electron is emitted as a β particle, and the nucleus transforms into magnesium-22 [58]. The decay equation is:



where, $^{22}_{11}\text{Na}$ and $^{22}_{10}\text{Ne}$ represent Sodium-22 and Neon-22 respectively, e^+ is the positron (anti-electron) and ν_e , the neutrino. The average energy of the positron is 215.5 keV and its maximum around 545.6 keV [59]. The asterisk (*) denotes that the Neon-2 is in excited state, and to transition to its ground state, it emits a γ photon of energy 1275 keV. Moreover, when the positrons (β^+) emitted by Sodium-22 encounter electrons, they annihilate each other, each pair producing two γ rays of energy 511 keV [60]. These γ emissions are often considered secondary processes.

5.1.5 Data acquisition

With the help of Anton Kristensen at the Physics Department of Aarhus University, using dosimeters and some heavy Lead blocks, we conducted a camera irradiation experimental set-up. The camera's lens was covered with black tape to block the light and the detection script followed the logic described in 2.2. The CMOS camera is connected to a Coral Dev Board Mini (as part of the DISCOSAT-1's IPU). The board is connected to a power supply Direct Current (DC), and the data are transferred to a Personal Computer (PC) Laptop through an Secure Shell protocol (SSH) connection. The block diagram of the experimental set up is depicted in 5.1. In the first round, we aimed to gather some α and β particle detection images from ^{238}U and ^{207}Bi sources respectively. Starting with ^{207}Bi source, the distance was decreased gradually to 0.5cm and managed to get around 100 detection counts. Keeping the same distance for irradiation using the ^{238}U source gave around 190 detection counts. Example of the irradiation set up can be seen in figure 5.2. At a later stage, we repeated these experiments, by exposing the camera to different radiation sources in a similar set up, aiming to get some γ ray detections and increase the overall amount of data. By the end of this round of experimentation, we managed to gather 154 detections from ^{22}Na , but only 46 from ^{60}Co .

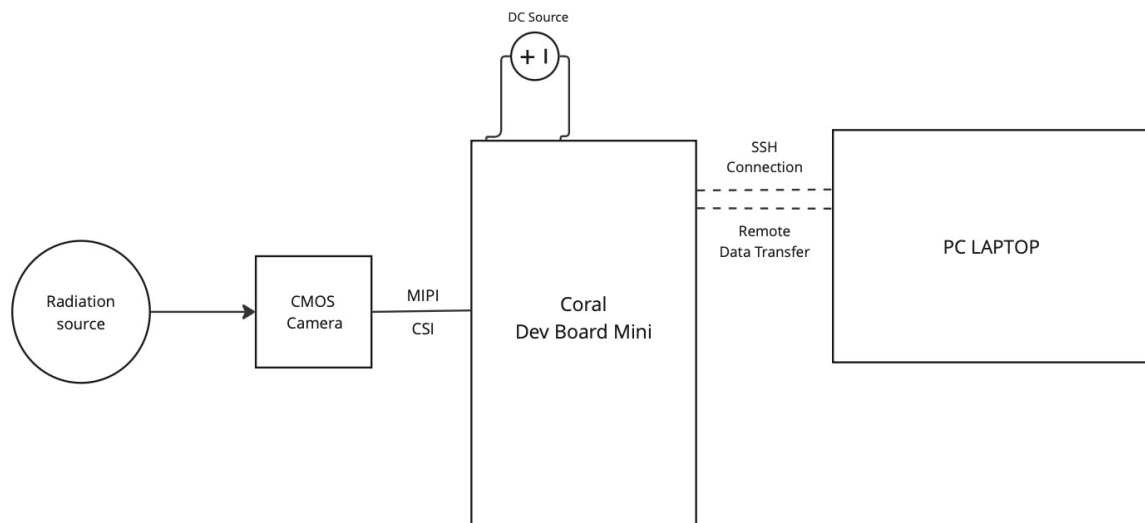


Figure 5.1: Block diagram of the experimental set up.

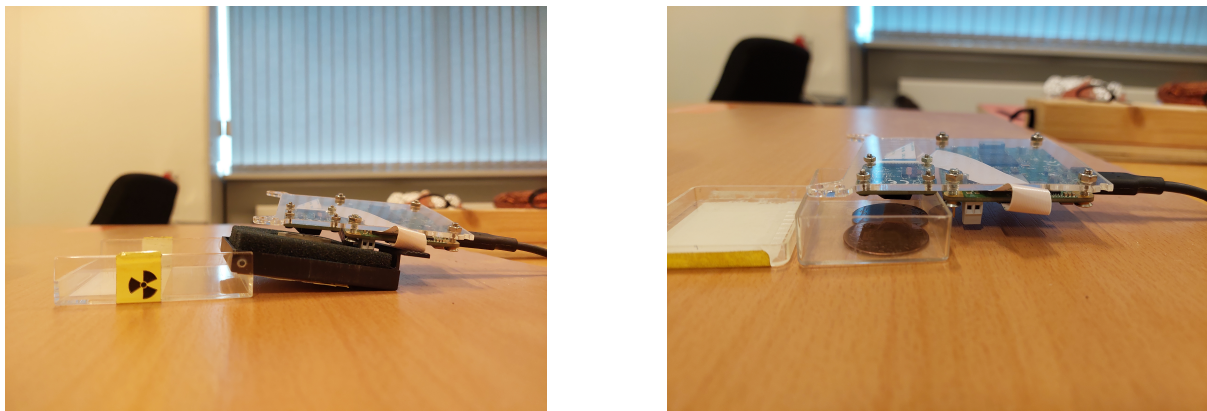


Figure 5.2: Camera irradiation set up.

5.1.6 Data analysis

The image processing involved grey scaling, binary thresholding and segmentation using contours by OpenCV as shown in figure 5.3. As mentioned before, for the first round of camera irradiation experiments, the ^{238}U and ^{207}Bi sources were used. These experiments were conducted under the assumption that ^{207}Bi and ^{238}U are primarily β and α emitting sources respectively. Therefore the initial goal was to analyse the data from these two sources, and extracting features that would aid in classification between α and β particles. The features

selected, aim to derive the energy deposited to the sensor from the radiation particles. Activated pixels refer to the number of pixels that were activated from the interaction, and the pixel intensity responds to the pixel value of each activated pixel.

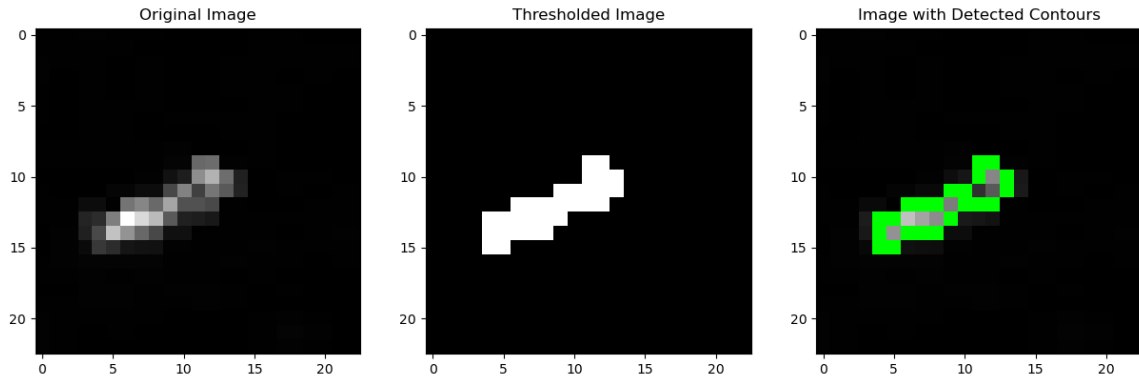


Figure 5.3: Single particle detection sample and its contour.

Taking into account the much larger mass and energy of the α particles, the logical assumption is that the charge deposited in the sensor would be higher in terms of pixel intensities. In order to understand how these particles differ in their interactions with the sensor, plotting the histograms for each features would be a good place to start. The figures 5.4 show the detailed histograms for the number of activated pixels, average, maximum and total pixel intensities categorised as α and β datasets.

The histogram of the number of activated pixels suggests that α result in fewer activated pixels per detection compared to β particles, which indicates that they have a more localized interaction with the sensor. On the other hand, β show a wider range of activated pixels causing more widespread interactions, which could be explained by their higher penetration power. Additionally, α seem to have a narrower distribution of maximum intensities, generally peaking at lower values. The β distribution, extends to much higher maximum intensity values, suggesting that some β particles produce intense interactions. The total intensity values of the α particles are concentrated at lower levels, which is consistent with the overall fewer and less intense pixels activated and indicates a more confined energy deposition pattern. β particles display higher total intensity values spread over a wider range, suggesting more extensive and varied interactions with the sensor. The distribution of average intensity the α dataset has a low

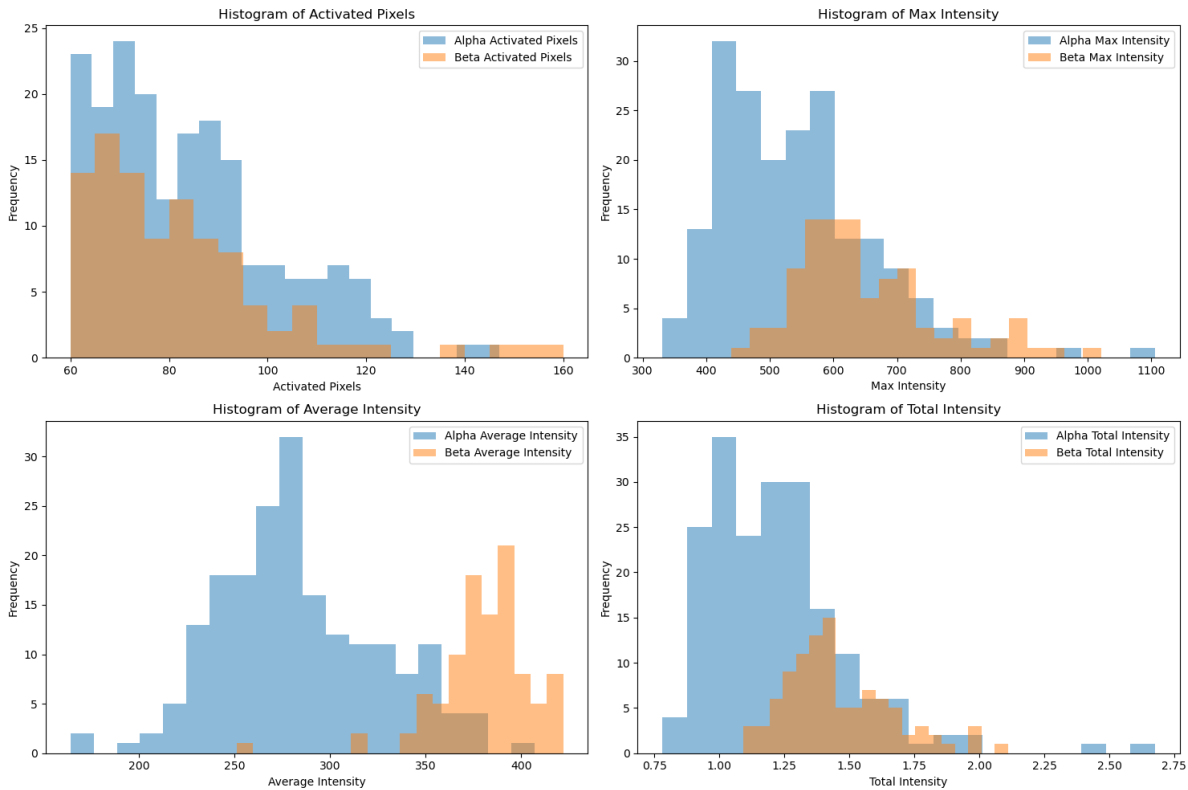


Figure 5.4: Histograms for activated pixels, average, maximum and total pixel intensity for ^{238}U (α) and ^{207}Bi (β) sources.

skew with peak value of around 250, whereas in contrast, the dataset shows a broader distribution and peaks around 325. It is expected that α particles produce a more intense signals per interaction, since they are heavier and possess more energy per particle.

There are few possible explanations to consider from this observation. α have a very short range in solid materials and might not penetrate deeply into the sensor, that could limit their energy deposition to a shallower layer. Accordingly, the lighter β might interact more extensively leading to broader signal generation across more pixels. Since γ rays are generally emitted during radioactive decays, another possibility could be that these particles are secondary γ photons, even if there are not directly emitted during the primary α decay process according to theory [55]. Nonetheless, if the daughter nucleus is in an excited state, it may release excess energy through γ ray emission in order to reach a stable ground state. Most of these γ rays have energies less than 500 keV [54].

The scatter plot of total intensity versus activated pixels in figure 5.5 represents a preliminary investigation on the potential for classification between α and β particles data from these sources. It also aids in investigating the proportion of the sensor area that is affected by an

interaction. The data points for α particles predominantly cluster in the lower left section of the plot. This cluster shows a range of total intensity values from approximately 400 to 800 and a range of activated pixels from about 200 to 350. This indicates that α particles typically activate fewer pixels and result in lower total intensity. This is contradictory to the expected outcome. α particles deposit a lot of energy in a small area, which means fewer pixels were expected to be activated, but with higher total intensity. Similarly, β particles should spread their energy over a larger area, meaning more activated pixels but with lower total intensity. However, this cluster displays total intensity values from approximately 500 to 1100 and activated pixels from about 300 to 450. This clustering implies β that particles generally activate more pixels and produce higher total intensity, which contradicts with theory. Furthermore, the α and β clusters overlap in the mid-range of total intensity (500-700) and activated pixels (300-350). This overlap indicates some conditions under which the responses to α and β particles are similar, potentially complicating straightforward classification.

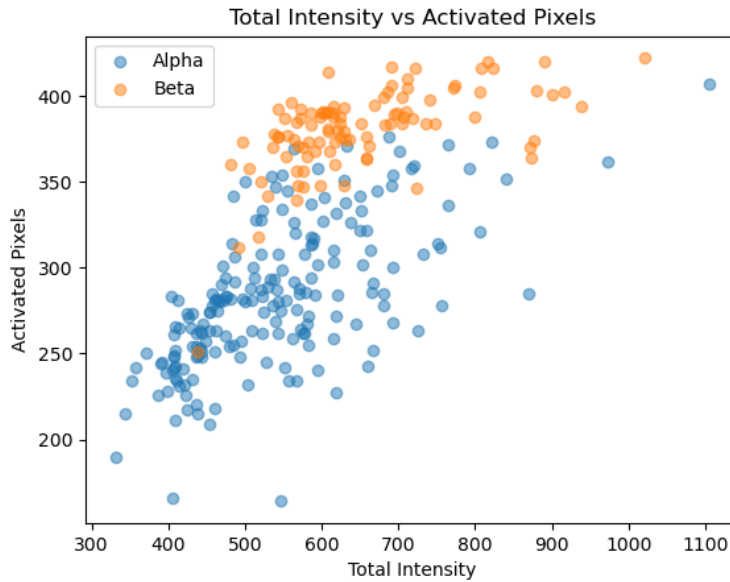


Figure 5.5: Scatter plot of total pixel intensity vs activated pixels for α and β source.

On the second round of irradiation, we exposed the camera to ^{22}Na and ^{60}Co radiation sources to acquire γ ray detection images. Figure 5.6 demonstrate the sample mesh plots of single particle detections from each source. There are some distinctive differences and similarities between these particle detections, in regards to the shapes and the pixel intensities they reach. The γ rays have longer and more sporadic tracks, oppositely to the α and β particles. Other meshes from literature review verify these shapes [39]. β particles however seem to have

much higher maximum intensity than the α which could be considered outliers, and this is also shown in the previous scatter plot 5.5 .

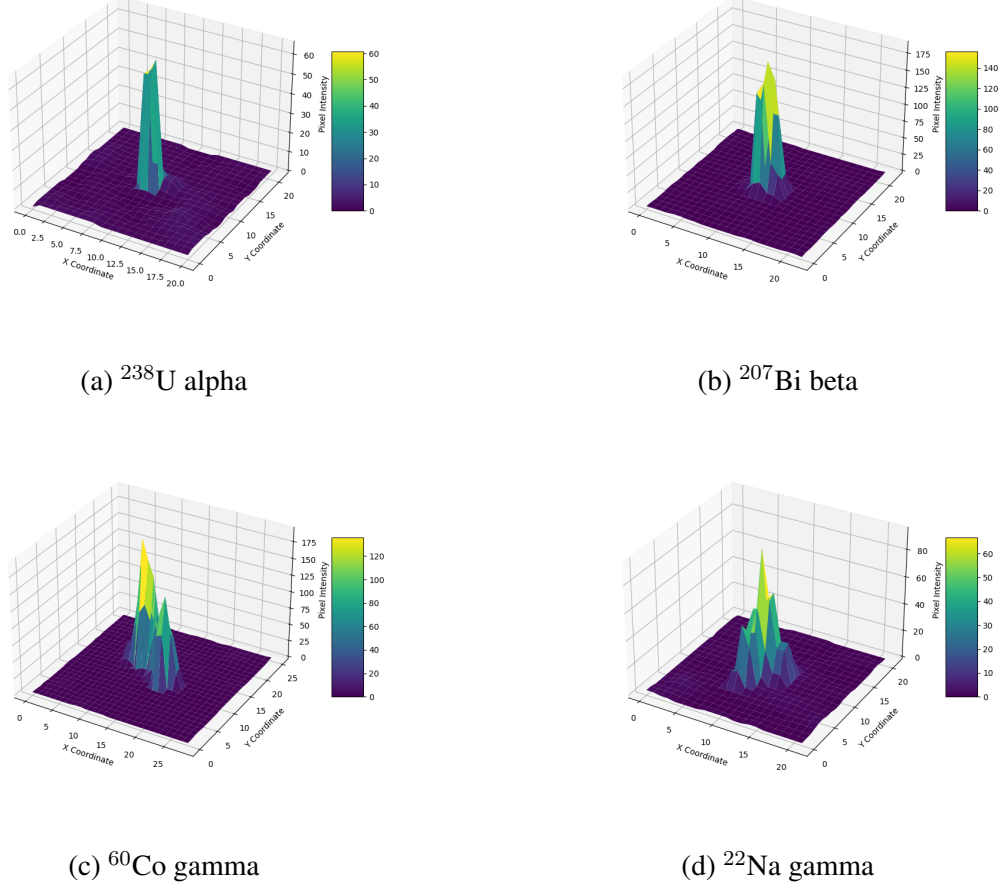


Figure 5.6: Mesh plot of a single particle detection from each source.

Source	Particle	Detections
Uranium-238	α	227
Bismuth-207	β	282
Cobalt-60	γ	42
Sodium022	γ	140

Table 5.1: Table of acquired experimental data.

Table 5.1 displays the amount of data acquired from each radiation source. These are the total (isolated) single events detected using the Cosmic Ray Detector script that can be found in the appendix .1.1. This unbalanced dataset between classes, is analysed at the rest of this section.

For a more comprehensive overview and comparison of the data across all data sources, figure 5.7 shows the Cumulative Distribution Functions (CDF) for activated pixels and total

pixel intensity for each source. In 5.7a, the Uranium-238 source shows the more concentrated distribution at lower activated pixels, meaning the smallest number of activated pixels. The Bismuth-207 source shows a moderate distribution of activated pixels, but fewer number of activated pixels compared to the Sodium-22 and Cobalt-60 sources. The distributions of these mainly γ sources , are similar and show the broadest distributions, with higher counts of activated pixels than the rest. The total intensity CDF plot provides insight into how the total intensity distributions differ among the sources, which is essentially a more comprehensive measure of how much energy is being deposited in total. The detections from the α source concentrate their energy deposition in fewer pixels in comparison other sources, which aligns with their high ionization potential over a short distance. The distribution line of the total intensity of the detections from the β source rises more gradually, indicating a wider spread of values. Similarly to their activated pixels distribution, γ rays show the highest and broadest overall intensity that reflects their low ionization and high penetration ability. Incorporating the physical qualities of α , β , and γ rays, the CDF graphs reflect their expected behaviors in terms of pixel activation and total intensity deposition.

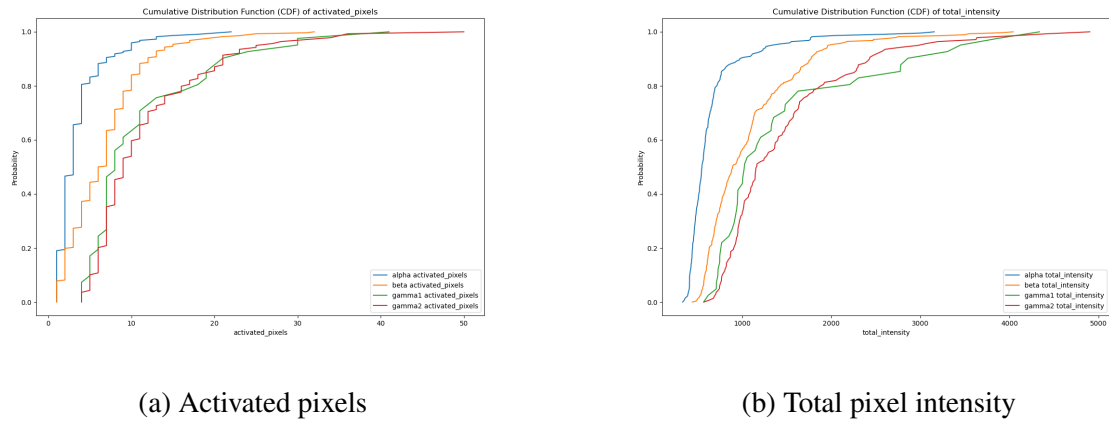


Figure 5.7: Cumulative Distribution Functions (CDF) for the different features.

Besides the pixel intensity and activated pixels features, it is also worthwhile to examine the particle tracks as a possible distinguishable feature for classification. The box and swarm plot figure in 5.8, visualizes the distribution of track lengths for the four different radiation sources. The track of each particle path is measured using the cv2.arcLength function, which calculates each contour's perimeter. This feature essentially represents the extent of the particle's trajectory. The data from Uranium-238 source, show a relatively narrow distribution of track

lengths, mostly concentrated between 0 and 10 units. The median track length for Uranium-238 is low and with a small range, indicating that most α tracks are short and closely clustered. The track lengths for Bismuth-207 show a wider distribution compared to Uranium-238, with values ranging up to approximately 20 units. The median track length is higher than Uranium-238, indicating a broader variation in track lengths. Last but not least, Cobalt-60 exhibits a broad distribution of track lengths with many tracks extending beyond 30 units and some outliers reaching up to 50 units. The median track length is significantly higher with much larger range which implies a considerable variability and longer tracks. Similar to Cobalt-60, a wider range of track lengths is showed for Sodium-22, with values extending beyond 30 units including outliers that reach up to 40. The median track length is also high, indicating a broad distribution of longer tracks. Overall, the track length measurements and interpretation of the plot align with the known physical properties of these radiation types.

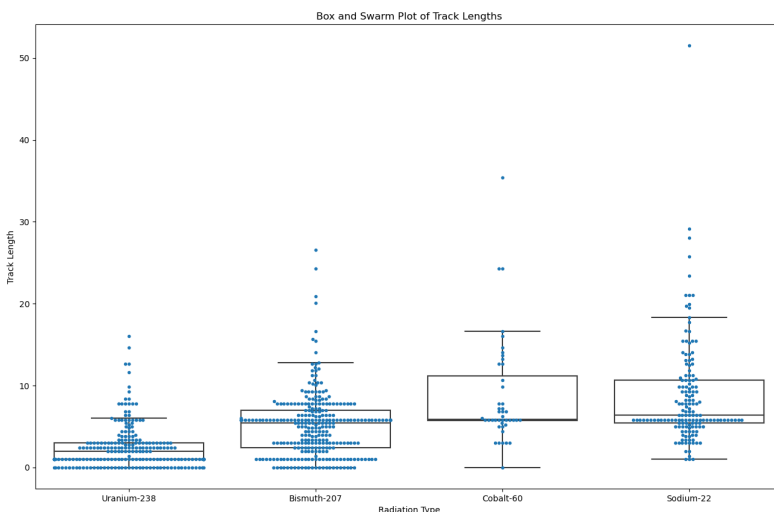


Figure 5.8: Box and Swarm Plot of Track Lengths for all sources.

Principal Component Analysis (PCA) is a powerful technique on gaining deeper insights on the given data structure. PCA transforms the original high-dimensional data into a smaller set of uncorrelated variables, called principal components, which retain most of the variance in the data. By reducing the dimensionality of the feature space, this process can enhance visualisation, reveal clusters and show the separability of the classes. It is also prone to filter out noise and redundant features. The PCA process starts by centering the data with subtracting the mean of each feature:

$$X_{\text{centered}} = X - \mu$$

where X is the original data matrix and μ is the mean of X . Then the covariance matrix of the centered data is computed and decomposed into eigenvalues and eigenvectors:

$$\Sigma v = \lambda v \quad \text{where} \quad \Sigma = \frac{1}{N-1}(X - \mu)^T(X - \mu)$$

where N is the number of data points, X is the original data matrix, μ is the mean of X , Σ is the covariance matrix, λ are the eigenvalues and v are the eigenvectors. Then the original data are projected onto the principal components (eigenvectors) corresponding to the largest eigenvalues:

$$X_{\text{reduced}} = X_{\text{centered}} V_{\text{selected}}$$

where X_{centered} is the data matrix after centering, V_{selected} is the matrix of selected eigenvectors and X_{reduced} is the data matrix projected onto the principal components [61]. The main goal for this analysis is to extract the most important features for classification. Figure 5.9 shows scatter plots between different principal components of the distribution of different classes in the reduced-dimensional space. There is a significant degree of overlap between the classes, that indicated that the classes are not perfectly separable in the PCA space. However, certain combinations of principal components demonstrate better separation which means that some inherent class structure remains. The overlap between classes suggests that a simple linear classifier might not suffice, and more complex models or preprocessing methods are required classification with higher accuracy. Considering the experimental method of acquiring these data, and thus the high uncertainty of the particle labels from each source, the investigation of each class seems appropriate. For example, as mentioned before α particles have a very short range in air, hence are easily stopped by a few centimeters of air or a sheet of paper. There is a high chance that the camera's lens stops α particles from reaching the CMOS sensor. The case around the lens is also made of metal, which would also provide a stopping power against these particles.

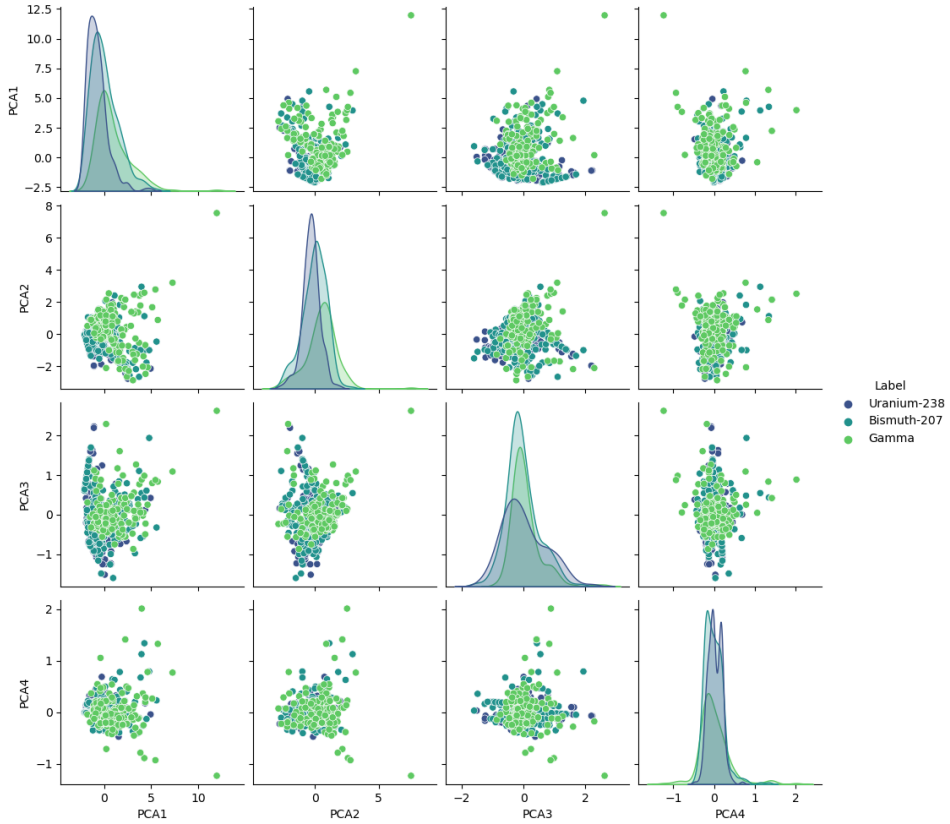


Figure 5.9: Principal Component Analysis on the whole dataset.

This also draws back to the each source's complex principles of radiation decay and each particle's intensity probability within each source. The particles with highest probabilities of emission for ^{238}U are indeed α of energy 4198 keV with 79%. There have been data suggesting the emission of X-rays with intensity 25% [62], while other tables show the intensity as low as 2% and 3% [63]. Both sources mention γ rays but at very low intensity levels and at low energies. As mentioned before, γ rays are also produced as secondary radiation during interactions with other surrounding materials. Unsupervised learning could be beneficial for aiding with the problem of labelling through clustering.

GMM is a generative probabilistic model that could be an effective tool for differentiating particles from the image detections derived from the same radiation source. They are broadly used due to their robustness to noise and variability in modeling complex, overlapping data distributions. The model assumes that the data are generated from a mixture of several Gaussian distributions. [64]. The model fitting process involves the Expectation-Maximization (EM) algorithm, which computes the probability (responsibility) that each data point x_i belongs to each component (cluster) k :

$$\gamma_{ik} = \frac{\phi_k \mathcal{N}(x_i | \mu_k, \Sigma_k)}{\sum_{j=1}^K \phi_j \mathcal{N}(x_i | \mu_j, \Sigma_j)}$$

In the M-step, the parameters of the Gaussian components are updated using the responsibilities:

$$(\phi_k, \mu_k, \Sigma_k) = \left(\frac{1}{N} \sum_{i=1}^N \gamma_{ik}, \frac{\sum_{i=1}^N \gamma_{ik} x_i}{\sum_{i=1}^N \gamma_{ik}}, \frac{\sum_{i=1}^N \gamma_{ik} (x_i - \mu_k)(x_i - \mu_k)^T}{\sum_{i=1}^N \gamma_{ik}} \right)$$

where γ_{ik} is the responsibility of component k for data point i , ϕ_k is the weight of component k , $\mathcal{N}(x_i | \mu_k, \Sigma_k)$ is the Gaussian density for component k , μ_k and Σ_k are the mean and covariance of component k , K is the number of components, and N is the total number of data points [65]. The resulting GMM clustering model for the detections captured from the Uranium-238 source can be shown in 5.10. PCA has been employed in this visualization to reduce the dimensionality of the feature space into two components, enabling the construction of a 2D scatter plot. Pairwise relationships between features aid in the investigation of the feature interactions for each cluster. If we assume α could have been detected, cluster 0 likely represents α particles due to their short, dense tracks and lower overall intensity. Cluster 2 is characterized by longer, less dense tracks and higher total intensity that suggests higher energy γ ray tracks. Cluster 1 however, is neither as localized and intense as cluster 0 to suspect α particle interactions nor as penetrating and sparse as the properties of γ rays suggest. These characteristics reflect the moderate ionization potential and penetration ability of X-rays. The scatter plots provide a detailed visualisation of the relationship between different features. Total Intensity and Activated Pixels are highly significant features since they show clear and consistent separation between clusters. Length also demonstrates a strong differentiation between short-range and long-range particle interactions, while the width contributes to a lesser extent. The credibility of this clustering is still too uncertain and with quite a few outliers to derive any concrete labelling from it. Generally, it would be hard to classify without any other indication for labelling other than probabilistic clustering. This analyses is mostly a demonstrative solution to the mislabelling problem.

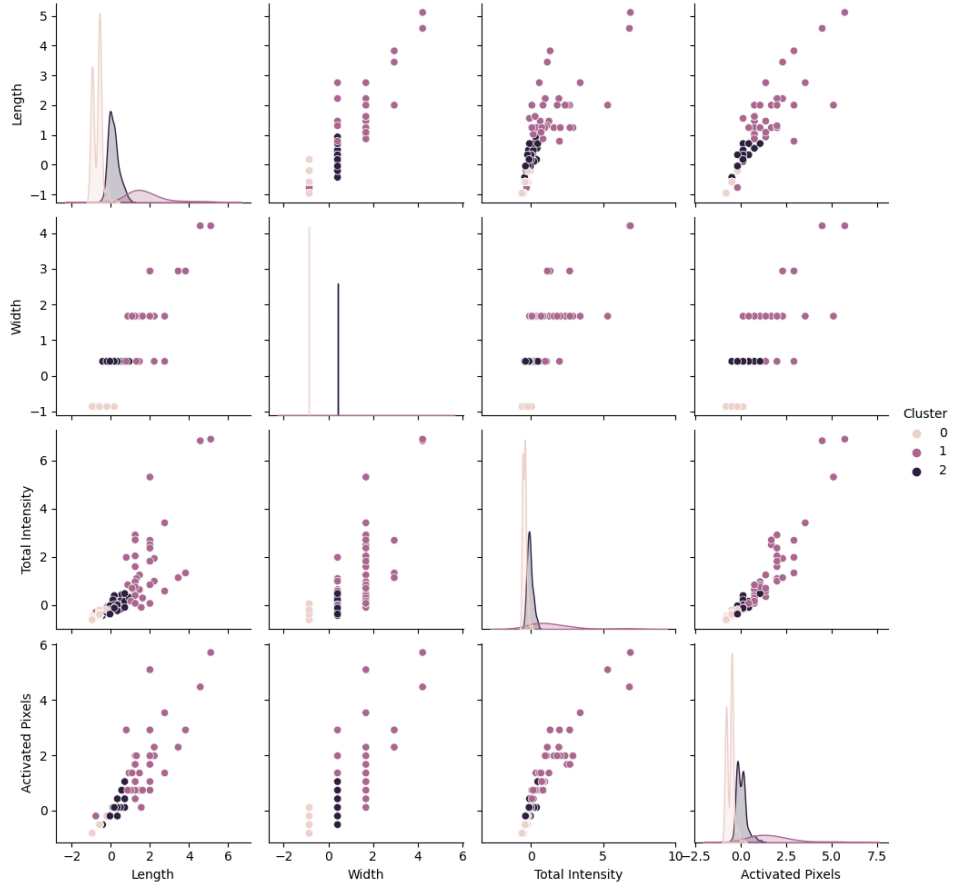


Figure 5.10: Gaussian Mixture Model for particles clustering in Uranium-238 source.

5.2 Proton beam experiment

The main objectives of this experiment lie in testing the camera's durability under high energetic protons (as relevant to cosmic rays), testing its performance as a dosimeter and the possibility of extracting information regarding the particles energy levels by obtaining a large enough dataset and utilizing machine learning methods for classification.

5.2.1 Data acquisition

The Danish Centre for Particle Therapy at Aarhus University Hospital has a dedicated horizontal beam room, available for internal and external research since October 2019. The beam consists of a horizontal proton pencil beam scanning (PBS), featuring an energy range of 70-244 MeV at a fixed 90° angle, a beam current on target ranging from 0.5 to 15 nA, a maximum field size of $30 \times 40 \text{ cm}^2$, a maximum dose rate of 10^6 MU/min , and a source-to-axis distance (SAD) of 228 cm [66]. The PBS system is designed for precise targeting and proton dose delivery in experimental setups that operated under specific parameters. The system adjusts the

energy of the proton beam (70-244 MeV) to control the depth at which the Bragg Peak occurs. The Bragg Peak is a fundamental concept in proton therapy, describing the behavior of protons as they travel through matter. Protons deposit most of their energy at a specific depth, known as the Bragg Peak, after which the energy deposition rapidly falls off [67]. This characteristic allows for highly targeted treatments with minimal damage to surrounding healthy tissues, which can lead to lower toxicity and better patient outcomes [68].

With the precious help of the researchers working in the hospital and the physicist Anton Kristensen, the camera was set up for proton irradiation as shown in 5.14. In this experimental setup, a proton beam is generated using a synchrotron and channeled through a beam line into a research target room. This operation is managed from a control room. A secondary wolfram target receives the beam, which diffuses it before it is columnated by a screen to maintain a precise beam width of about 200 mm. The entire setup is connected by a curved corridor linking the laboratory and target rooms. The camera is placed perpendicular to the beam and mounted on a 3D-printed plastic holder, positioned 1.60 meters away from the secondary target. This camera is linked to a Coral Dev Board Mini via a MIPI CSI-2 interface. The Coral board itself is connected to a Raspberry Pi via USB, and the Raspberry Pi is further linked to a laptop in the lab room through a CAT6 Ethernet cable, facilitating data transfer and remote operations. Control and data handling are achieved through a series of networked sessions and scripts: an SSH session runs from the laptop to the Raspberry Pi, and a screen session connects the Pi to the Coral board. The camera is triggered by Python scripts running on the Coral, and the acquired image data is initially stored on the Coral board. At the end of each experimental session, the Coral boards are removed, and data is transferred using Mendel Development Tool (MDT) shell over USB-C. Throughout the experiment, large acrylic blocks protect the electronic components by absorbing the protons, ensuring the integrity of the sensitive equipment and collimator are positioned to in between targets and the beam source, to limit the maximum field size of the beam. The simplified diagram of this set up is demonstrated in 5.11. The only difference of the detection software program used from the previous experiments is that it only saved the whole frames, when a particle is detected, instead of cropping and saving isolated events as we did in the previous experiments. Last but not least, safety protocol was followed through the experiments, conducted by the researchers with personal dosimeters and dose detection in the target room during and after each session.

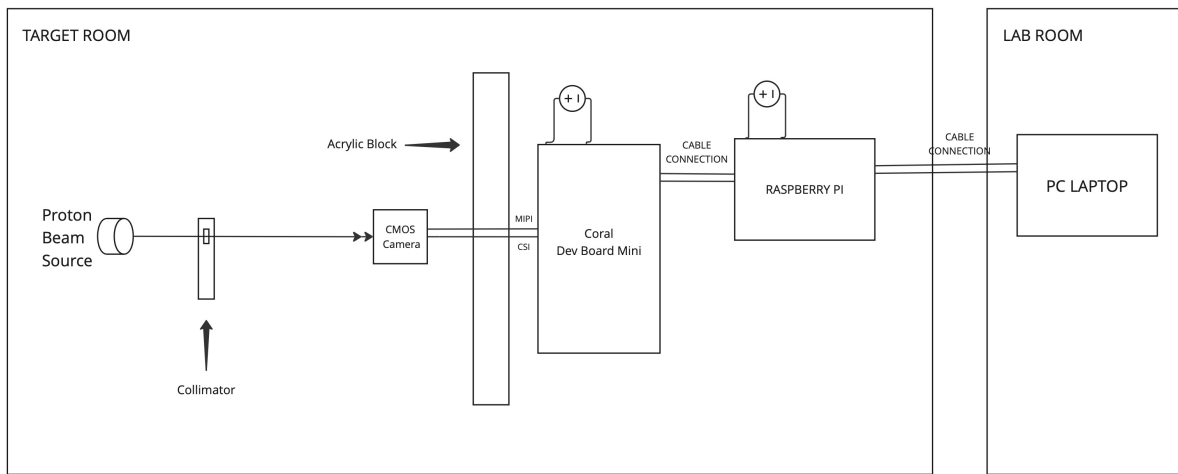


Figure 5.11: Simplified diagram of the proton beam experiment set up

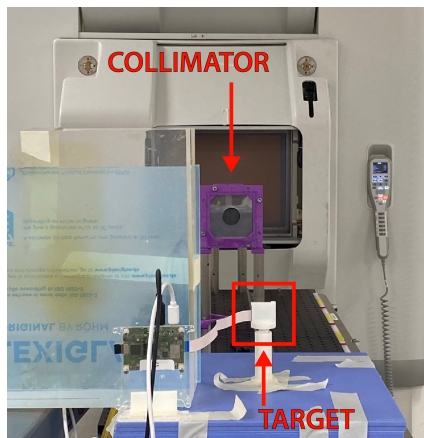


Figure 5.12: Front view

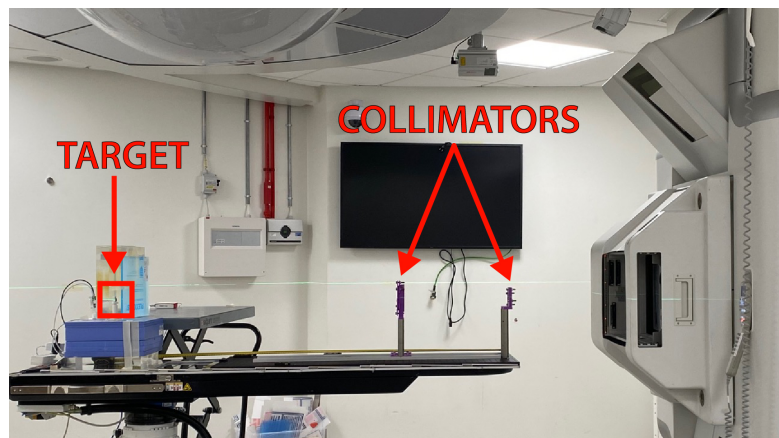


Figure 5.13: Side view

Figure 5.14: Experiment set up for camera irradiation using a pencil proton beam.

The table 5.2 demonstrates the log of the data acquired data from this experiment that includes timestamps, number of frames captured, the energy level (MeV), current (nA), dose measurement Monitor Unit (MU) and angled position of the camera for each run, along with some notes regarding materials used. MU is a measure used to quantify the amount of radiation delivered to a specific area by a radiation therapy machine, and is determined by the duration and intensity of the beam. Each MU corresponds to a specific amount of radiation absorbed, usually calibrated based on the machine's rate. The intensity of the proton beam for this experiment, corresponds to a proton flux of $5000 \text{ protons/cm}^2/\text{s}$. All images were captured by using 40 FPS, image resolution of 1920×1080 pixels and a threshold above 30. The table also

includes the logs of the holistic experimental procedure of changing angles and the added materials placed between the beam and the camera aimed to lower down the proton energy level reached at the target point (camera). The resulting proton energy levels at the target point are estimated by the researcher. The acquired images aimed to gather a range of different MUs and energies to utilize the data for dose and energy dependencies. Firstly, by keeping the energy at target static to 122 MeV and the dosage measurement unit was gradually increased from 1 MU up to 500000 MU. Continuously, the dose measurement stayed at 10000 MU and the energy levels were changed by placing absorbing layers in the beam path, as mentioned in the notes section of the table 5.14. Additionally, the camera was slanted at different angles to the beam. Last but not least, a saturation test was conducted by maximizing the energy at 244 MeV and 10000 MU. The saturation experiment concluded successfully, with the camera remaining unsaturated throughout the testing period. The values for the duration of irradiation have been derived from the logs provided by the hospital.

Timestamp	Frames	Energy (MeV)	Current (nA)	MU	Angle	Irradiation time (s)	Notes
20:20	2	122	50	1	0	0.003176	
20:22	2	122	50	1	0	0.004096	
20:23	1	122	50	1	0	0.003545	
20:24	1	122	50	10	0	0.035446	
20:25	2	122	50	10	0	0.037724	
20:25	2	122	50	10	0	0.036193	
20:26	3	122	50	10	0	0.030190	
20:27	4	122	50	100	0	0.385419	
20:28	4	122	50	100	0	0.343228	
20:29	4	122	50	100	0	0.288918	
20:30	3	122	50	100	0	0.325158	
20:31	15	122	50	1000	0	4.614140	
20:33	13	122	50	1000	0	3.716517	
20:35	12	122	50	1000	0	3.369682	
20:36	13	122	50	1000	0	3.798539	
20:40	108	122	50	10000	0	40.391946	
20:45	114	122	50	10000	0	43.581761	
20:55	0	0	0	0	0		Board change
21:03	93	33	50	10000	0	36.543723	10cm solid water
21:09	101	23	50	10000	0	38.945911	10.5cm solid water
21:12	70	5	50	10000	0	26.922387	11cm solid water
21:15	70	-	-	-	-	30.297762	13cm solid water //only products
21:29	96	122	50	10000	60	36.503873	
21:32	103	122	50	10000	80	39.331212	
21:39	98	122	50	10000	0	37.007311	
21:41	10	122	550	10000	0	3.187161	
21:43	0	0	0	0	0		Board change
22:01	449	122	50	50000	0	168.244086	
22:05	486	122	50	50000	0	187.607259	
22:10	6	244	50	10000	0	2.000186	

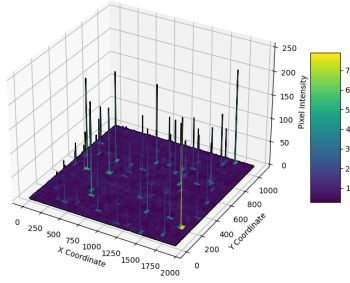
Table 5.2: Proton beam experiment log table

5.2.2 Data processing

This section describes the image processing techniques, limitations and goals. The general goal is to extract valuable information from the images for analysis, regarding how the sensor responds to high-energetic protons. The main focus is to segment the particle events in order to count them for dose measurement purposes. Since a lot of similar works suggest that camera irradiation usually causes a patterned noise in CMOS sensors [30], [40], [39], the software used in these experiments captures an initial frame before each irradiation run. The histograms of these frames showed that the noise was minimal with low frequency and a higher value of 10. The initial frames were meant to be subtracted from the detection frames but since a lot of these included some secondary radiation particle detections (caused by the radiation exposure of the target room), this step has been skipped. It's also important to notice that these

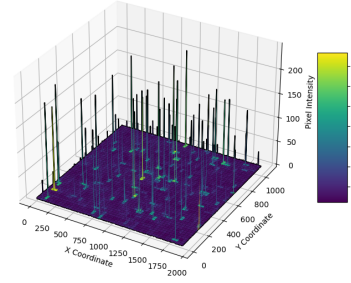
are not raw RGB data to be considered demosaicing processing or other advanced processing methods. DISCOSAT-1 wouldn't be able to downlink raw data or full frames (unless under a strong compression) and its IPU was design to deliver counts or at most, transfer small cropped images of a few pixels, as the Cosmic Ray Detector was also designed to do. The algorithm described below is processing full frames for segmentation, resulting in total particle counts per frame. Mesh plots were created as a first inspection of the detection frames for the different energies of the dataset, and they are displayed in 5.15. The energy deposited to the sensor for 244 MeV frame seems much higher than the rest, suggesting that the camera might start to saturate at that energy level.

Pixel Intensity Values for 5.5 MeV frame



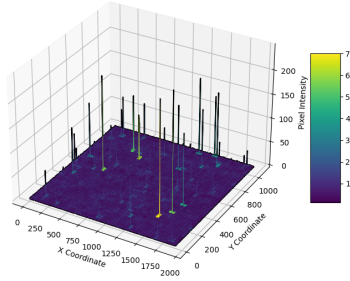
(a) 5.5 MeV frame

Pixel Intensity Values for 23 MeV frame



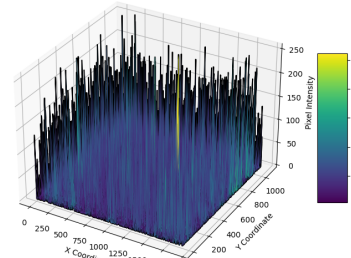
(b) 23 MeV frame

Pixel Intensity Values for 122 MeV frame



(c) 122 MeV frame

Pixel Intensity Values for 244 MeV frame



(d) 244 MeV frame

Figure 5.15: Mesh plots of sample frames for energy classes.

The software used in the initial experiments for isolating the events was not working efficiently due to the high density of events in multiple frames. After experimenting with various processing and segmentation techniques, such as morphological operations and watershed segmentation, the most efficient approach was found in a suggestion in stackoverflow [69] and it

has been implemented with adjustments throughout the data analysis of the acquired data from this experiment for particle counting. An example for deriving the particle counts in csv files can be found in the appendix .1.9. K-means color quantization is simplifying the representation of the image by reducing the numbers of colours. This process involves clustering pixel colors into k groups and replacing each pixel with its cluster's centroid color. The key steps include calculating the Euclidean distance between each pixel and the cluster centroids as shown in the equation:

$$d(x, c) = \sqrt{(R_x - R_c)^2 + (G_x - G_c)^2 + (B_x - B_c)^2}$$

where R_x, G_x, B_x are the RGB components of the pixel x and R_c, G_c, B_c are the RGB components of the centroid c . Then based on that computed distance, each pixel is assigned to the nearest cluster by:

$$\text{label}(x) = \arg \min_k d(x, c_k)$$

where $\text{label}(x)$ is the cluster assignment of pixel x , and c_k is the centroid of cluster k . The centroids are recalculated as the mean of all pixels assigned to each cluster:

$$c_k = \frac{1}{N_k} \sum_{x \in C_k} x$$

where c_k is the updated centroid of cluster k , N_k is the number of pixels assigned to cluster k , and C_k is the set of all pixels assigned to cluster k .

The algorithm converges if it reaches the maximum number of iterations specified (10000), or if the movement of the centroids drop below a threshold value (0.0001) and it is expressed through:

$$\text{converged if } \|c_k^{(t)} - c_k^{(t-1)}\| < \epsilon \quad \forall k$$

where $c_k^{(t)}$ is the centroid of cluster k at iteration t , and ϵ is a small threshold value. In this application, k-means is performed with two clusters to create a grayscale image and Otsu's thresholding is for binarization. After filtering out tiny noise, using contour area filtering and a mask is created to erase it. Bitwise-operation applies this mask to the original image, resulting in significant particle clusters [70], [71], [72]. The number of particle counts and average particle size computed from this algorithm are saved in a csv file for further processing. The processing steps are visualised in figure 5.16 for each of the different energy level classes.

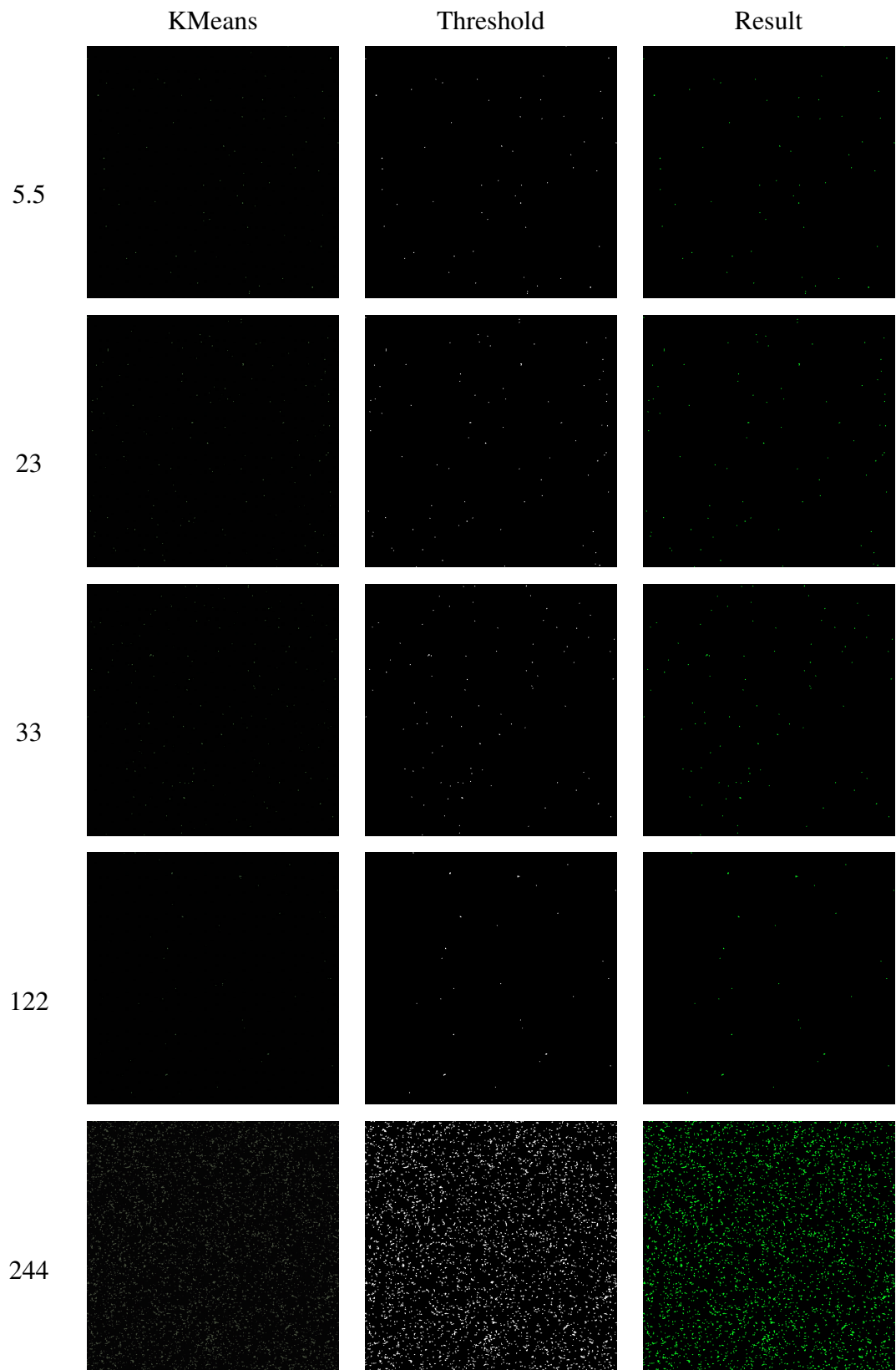


Figure 5.16: Image segmentation steps with samples from each Energy Level Class (MeV).

5.2.3 Data analysis

This section is focused on the characterization of the camera using the data from the proton beam experiment. The first subsection is concerning the camera's capability of measuring the dose delivered to the sensor using different feature extractions. The second subsection explores the how the camera sensor responds to different energy protons, by keeping the dose rate constant.

5.2.3.1 Dose measurement

As mentioned in 5.2.1, MU refers to Monitor Unit, which a measure used in radiation therapy to quantify the amount of radiation delivered to a specific target area. This metric is used throughout this section as interchangeable metric for dose measurement in order to analyse the camera's dosimeter capabilities. Working with the image data for different MU values 1-50000, with constant energy level at 122 MeV, expecting to see a somewhat linear relationship of the increased dose rate. Simultaneously, this section explores the different features that can characterize the camera sensor's response to proton radiation and their efficiency.

Figure 5.17 shows the total activated pixels and total pixel intensity against the different MU classes. Each data point represents the sum of all activated pixels per run. These plots do not show a linear relationship but there is an curved increase as initially suspected. Since this increase can be interpreted as exponential, transforming these graphs into a logarithmic scale seemed reasonable. The following figures 5.18, express the average activated pixels and total intensity per run by MU, but in logarithmic scale. To ensure that the x-axis values are spaced proportionally to their actual values, the distance between each tick on the x-axis should reflect the true differences between the values they represent. For example, the distance between 1 and 10 should be equal when using a logarithmic scale. These plots showcase a proportional relationship between these features and the MUs, with a general indication that the camera can be used as dosimeter accurately.

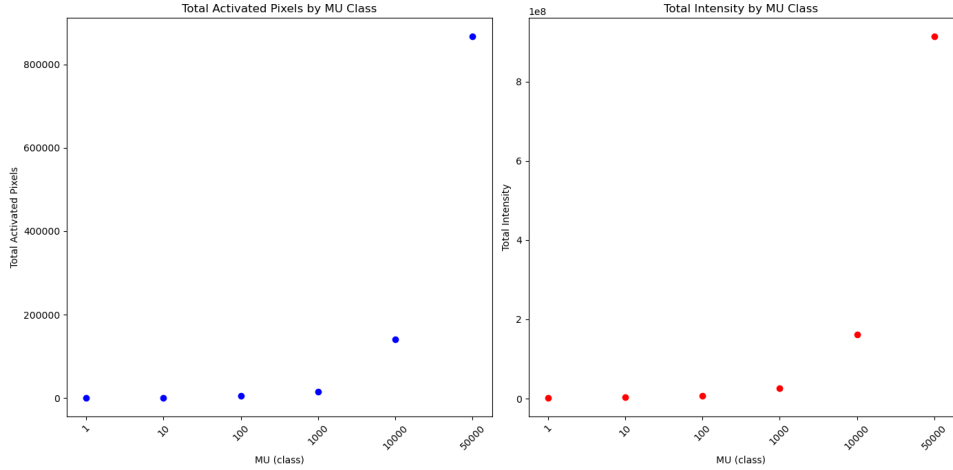


Figure 5.17: Total activated pixels and total intensity against Monitor Units (MU).

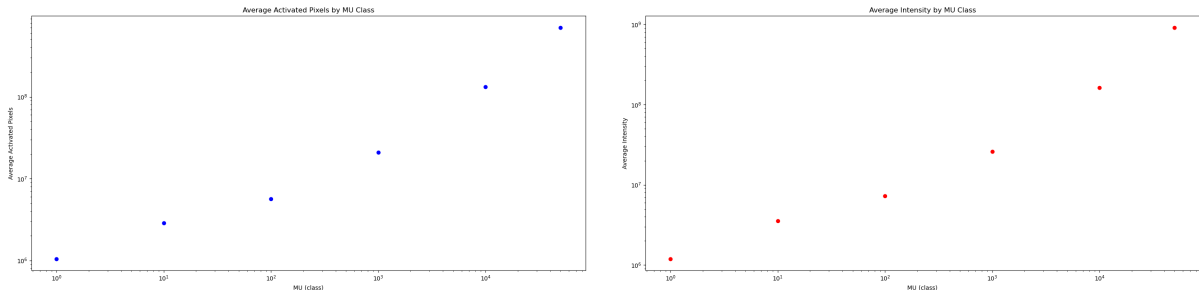


Figure 5.18: Average activated pixels and average intensity (log) by MU.

The table in 5.3 shows the total counts for each MU class at the same energy level (122 MeV). The algorithm used for the extraction of particle tracks is described in 5.2.2. The total count for each class has been calculated by adding the total counts frames for each run. While the particle counts increase dramatically while MU increases, the change in average particle size is negligible.

MU Class	Number of Frames	Total Particle Count	Avg Particle Size
1	1	22	2.227
10	2	84	3.194
100	4	428	3.784
1000	15	1327	3.723
10000	108	12237	3.702
50000	449	85304	3.716

Table 5.3: Particle Count, Size, and Number of Frames by MU Class

The particle counts derived from the processing algorithm shown in table 5.3, should also reflect the increase in dose rate of the beam accordingly. The particle counts versus MU is

visualised in figure 5.19. The plot shows close to a straight line, that suggests a linear relationship between the MU class and the total particle count. This means that doubling the MU class would roughly double the particle count, confirming a proportional relationship. Since the first few MU values (1-1000) have a significant difference to the last one 50000, the second plot in 5.19 consists of a zoomed in version of these values, for a better visualisation. Even though, these values do not follow a straight line there is a definite increase of particle counts accordingly.

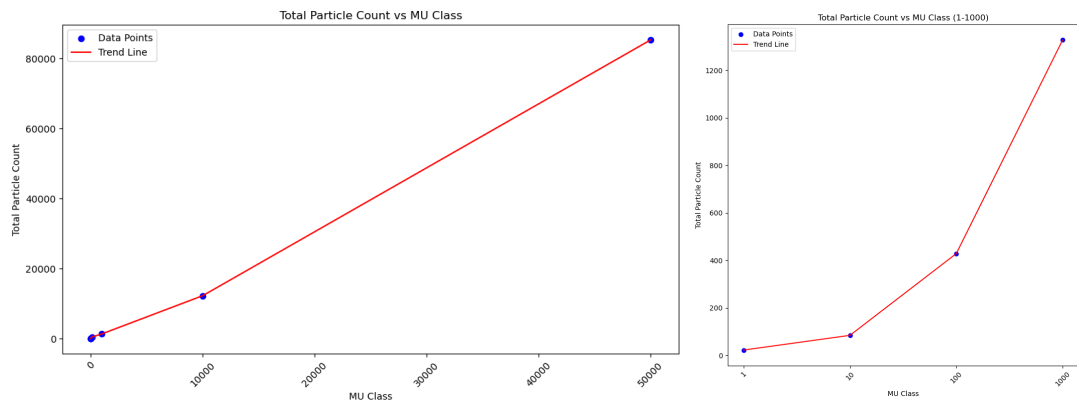


Figure 5.19: Total Particle counts for each MU Class (1 - 50000) and (1-1000) MU respectively.

To find the exact equation for the relationship between the MU class and the total particle count, linear regression is a good choice for modeling a linear relationship between variables. A defined linear equation is also useful in future predictions regarding new unseen data points, when available. The equation of the regression line can then be expressed as:

$$y = b^1 + b^2 \times x \quad (5.1)$$

where, y is the dependent variable (total particle count), x is the independent variable and b^1 , b^2 are the intercept and the slope of the line respectively. The line fit of particle counts versus MU is shown in figure 5.20 and the resulting linear equation derived is described as:

$$\text{Total Particle Count} = -814.30 + 1.71 \times \text{MU Class} \quad (5.2)$$

To evaluate the performance of the regression model, the statistical metric used is the Mean Squared Error (MSE). MSE measures the amount of error in the model by averaging the squared differences between the observed and predicted values, and its expressed with the equation:

$$\text{MSE} = \frac{1}{n} \sum_{i=1}^n (y_i - \hat{y}_i)^2$$

where y_i are the observed values, \hat{y}_i are the predicted values, and n is the number of observations [73]. The errors in MSE reflect the variance of the residuals. This regression model's high value of MSE indicates a significant error in estimating predictions. The potential reasons could involve high data variability, the presence of outliers or non-linear relationship. An important factor that can cause issues in this mode, is the very low amount of data used. Therefore, the need for more data to train this model is essential. Additionally, in order to properly evaluate this model, requires to analyse its performance also on unseen data. Assuming more data were available, the next step would also involve evaluating the model's performance on a separate validation and test dataset.

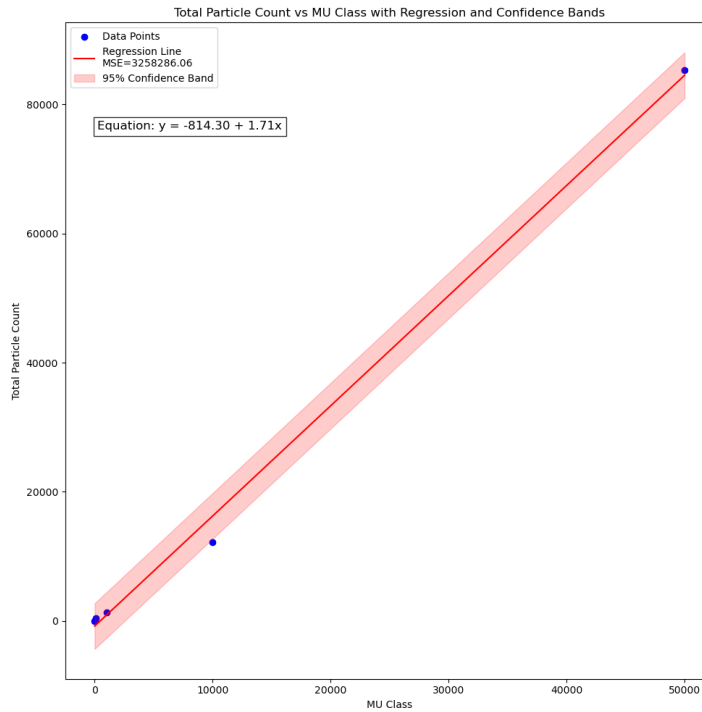


Figure 5.20: Total particle counts vs MU with Regression and Confidence Bands.

Another important element of this analysis belongs to the accurate dose measurement in regards to the number of proton expected versus the number of proton detected. This is an easy and straightforward way to evaluate the camera credibility as a dosimeter. The formula to calculate the expected number of protons is:

$$\text{Total expected protons} = \text{Flux} \times \text{Exposure Time per Frame} \quad (5.3)$$

The proton flux is been estimated as approximately 5000 protons/cm²/s for 1 MU. The FPS is 40 frames per second for these detection and the sensor's image area dimensions are known to be 0.1006 in cm² and gives:

$$\begin{aligned}\text{Total Expected Protons} &= 5000 \text{ protons/cm}^2/\text{sec} \times 0.1006 \text{ cm}^2 \times 0.025 \text{ sec} \\ &= 5000 \times 0.1006 \times 0.025 \\ &= 12.575 \text{ protons}\end{aligned}$$

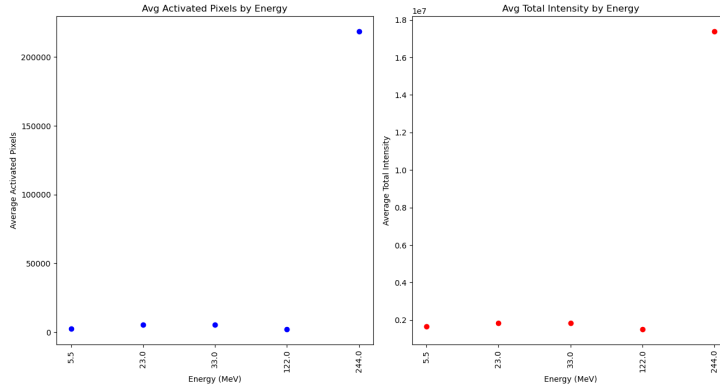
The CMOS camera is expected to capture 12.575 protons in that single frame as shown above. The detection algorithm detected 22 particles, that is almost double the amount. There is a high possibility that the processing algorithm considers small particle detections as noise and discards them. By lowering the area to be considered as noise, more particles were detected for all classes except the one that has been used in the equation 5.3.

5.2.3.2 Energy

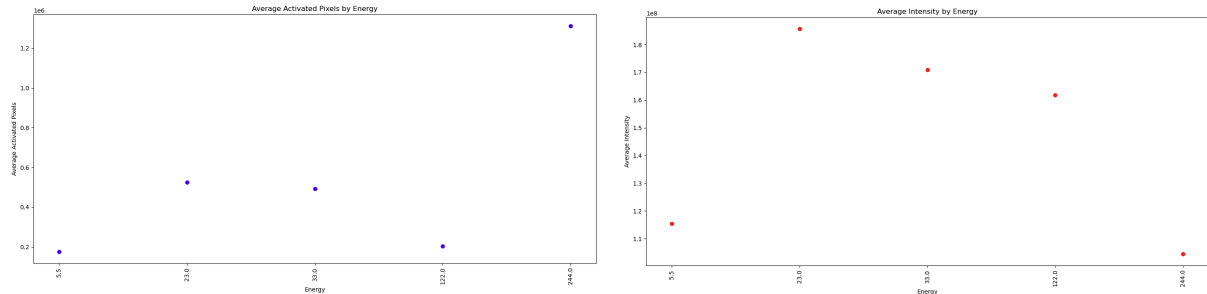
This section aims to investigate if there is any energy dependency on the image data. The CMOS camera is capable of detecting radiation particles, but there is no obvious indication that it can hold information on the particle's energy level. The initial plots in figure 5.21a show the average activated pixels and total intensity against energy. The data points illustrate the total sum of pixel values for one run at the same MU. The plot pinpoint similar pixel values with energy 23-33 MeV, a bit lower for 5,5 MeV but also lower at 122 MeV which seems counter-intuitive. While, at twice the energy level with 244 MeV, the activated pixels are enormously higher. This observation could imply that there might be a threshold energy level (between 122 and 244) at which the sensor responds differently. The average values of these features is used in these visualisations since their total and maximum had very similar if not identical results. The figures 5.21b and 5.21c represent the same average activated and pixel intensity features but in logarithmic scale. This initial analysis does not appear any distinctive correlation between pixel activation and the energy level of the particle. The data points are sporadic and inconsistent with the energy level spectrum.

Utilizing the algorithm described in 5.2.2, and a different analysis approach, figure 5.22 demonstrates the Kernel Density Estimation (KDE) plots, of particle counts and average size detected by the algorithm for each energy level across each run's frames. KDE is a statistical

estimate of the Probability Density Function (PDF) that does not assume a specific parametric form for the distribution. It instead uses a kernel function for smoothing the data points, producing a curve that represents the density. Essentially, it reflects how densely the data points are packed around the x value (particle count and average size). Class 122 has a distinct peak, indicating a highly concentrated distribution of particle counts, while Class 33 and 23 have more spread out distributions. Class 244 shows a flat line at the bottom, indicating that this class has very few particle counts across the range. The KDE plot for the average size particle shows that the classes with energies 33, 23 and 5.5 have tightly clustered particle size around 4, whereas class 122 suggests a binomial distribution. Class 244 has a wide spread of average particle sizes per frame and it stands out with its high variability.



(a) Average activated pixels and average intensity.



(b) Average activated pixels log

(c) Average pixel intensity log

Figure 5.21: Pixel intensity and activation plots against Energy in MeV.

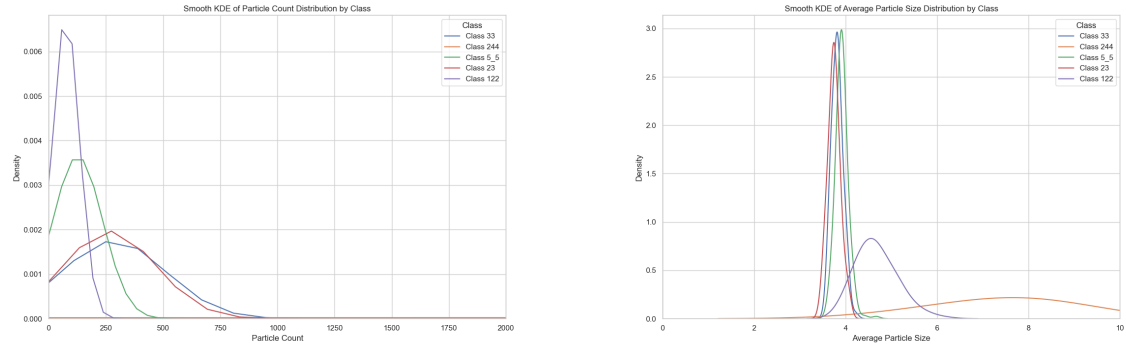


Figure 5.22: Smooth KDE for Particle Count and Average Particle Size Distributions for each Energy class in MeV.

Some frames across the image data have been observed to be "half" exposed to protons during irradiation with the proton beam suggesting that the camera has a rolling shutter. Showcasing how the particle counts change over time, could reveal distinct patterns and behaviours. The time-series plots for each energy class in figure 5.23 show the exact number of particles detected at each frame within each run. Class 5 shows initial volatility with particle counts starting low and then stabilizing around 150-175, reaching a consistent state. Class 23 generally exhibits greater variability, with counts ranging from 275 to 400 and a slight downward trend towards the end. This shows a more dynamic changes in particle behavior over time. Similarly to 5.5, class 33 initially, displays a clear upward trend, followed by a somewhat stabilization around the values of 350-400 counts. In contrast, Class 122 displays substantial volatility with counts fluctuating between 80 and 160 and no clear trend. This behaviour indicates a highly dynamic and unstable particle count change. Class 244 first frames have a very low count and suddenly jump into around 12000 counts, showing an extreme change.

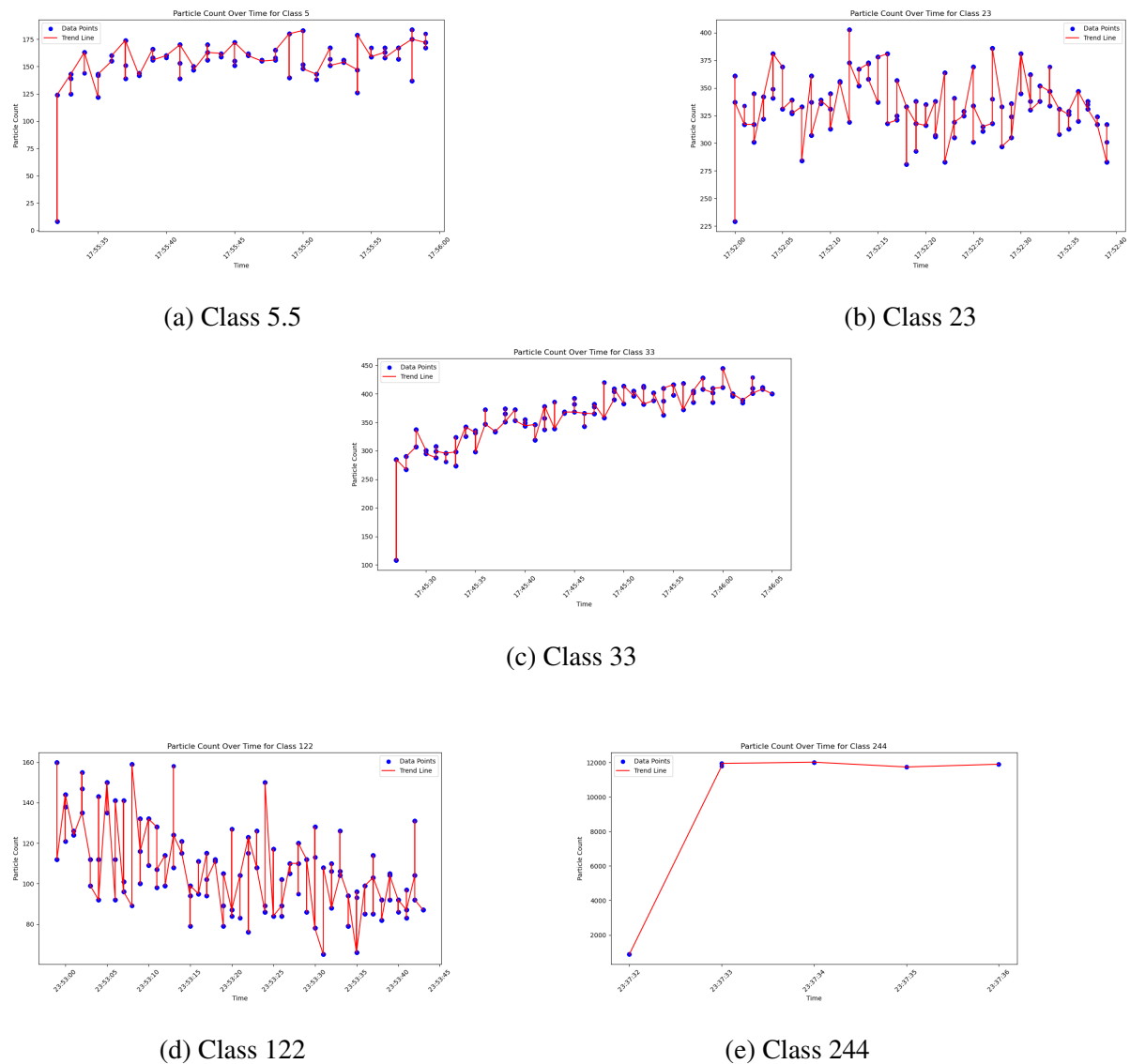


Figure 5.23: Particle counts over time for each energy class in MeV.

Chapter 6

Discussion

6.1 Irradiation experiments

The results from the irradiation experiments using various sources are promising regarding showing feature differences between different radiation particles. During these experiments they were a few assumptions made, with the most important simplification that each source producing one kind of radiation particle. This assumption was disproved and impeded the data processing and analysis process. The proper labelling of each particle detection could not be verified from either the decay equations nor the clustering visualisations by feature extraction. The initial analysis aimed to obtain 2 classes from Uranium-238 and Bismuth-207 sources, gathering α and β labelled particle detections, and investigate the features associated with the energy they deposit to the sensor. The analysis conducted suggested that most distinctive features that could be used for classification are activated pixels and average intensity. These features still showed some overlapping during clustering, with quite a few outliers as shown in 5.4 and 5.5. The reasonable explanation for this would be that since α particle have a very low penetration, they most likely are stopped by either the lens, or its surrounding case material before they reach the sensor. There is a strong indication that the particles detected from Uranium-238 are secondary radiation (most likely γ) produced by interactions due to α 's high amount of charge. As mentioned in 4 there have been many successful works on particle detection and classification using CMOS sensors, but these experiments were conducted under a very controlled environment. For example, during irradiation with ^{241}Am , the sensor's distance from the source (without a lens) was less than 5mm and the set up included shielding from other particles, making the dataset much more reliable [39]. Ensuring an accurately labelled dataset for each particle is a crucial step in developing and later evaluate a supervised machine learning model that this project does not include, due to the reliability of the experimentally acquired data.

Literature review declares that the particle tracks differ for each of these particles (α, β, γ) and the box and swarm plot in figure 5.8 suggests that there are distinctions between each source's track lengths. The boxes representing the interquartile range (IQR) show the 50% of the data to have different values across the different sources, but the outliers are also significant, (data points outer the box) which indicate variability within a radiation type. Moreover, the data from the Cobalt-60 are much less than the rest of the datasets, introducing more uncertainty. To address this issue, the data from Cobalt-60 and Sodium-22 were combined into a γ class in order to gain a bit more balanced dataset. PCA was conducted on these 3 classes representing the 3 different radiation particles in order to extract the most meaningful features between pixel intensity, activated pixels and track lengths and can be seen in 5.9. Even though this analysis shows a notable overlapping of these classes, some inherent class structure remains. This overlapped clustering suggests that linear classifiers wouldn't be appropriate for this classification problem. Furthermore, since the labels of these isolated events cannot be verified, unsupervised learning could simplify these problems and uncertainties. Following this method, GMM was modelled for the detections from the Uranium-238 source to evaluate if there is some natural clustering utilizing this powerful probabilistic algorithm. Figure 5.10 shows this clustering attempt using 3 classes and demonstrating the influence of each feature. This clustering result could be interpreted as the data points in cluster 0 to represent α particles due to short tracks and lower intensities, cluster 2 to belong to γ rays due to the highest intensities and longer tracks and cluster 1's data points under X-ray emissions. This is a very uncertain hypothesis that cannot be verified and the probabilities of the Uranium-238 source to emit X rays seems pretty low, even though scientific data are contradicted on these exact probabilities. This analysis did not extend to the rest of the datasets due to the high level of unreliability of attempting to label the events through unsupervised clustering. Another approach to this labelling problem would be to look for clear datasets of isolated events for the different particles and train a supervised machine learning algorithm on that dataset, and utilize the acquired data from this experiment as new unseen data. This could provide a more reliable labelled dataset. Generally, the analysis could not be conducted accurately without more reliable data and it would involve randomly chosen labels, thus it was not investigated further.

Overall, these irradiation experiments showed that the CMOS camera is able to successfully detect with no sign of degradation or saturation during irradiation. Contradictory to other similar works, minimal to insignificant noise was observed in the sensor after irradiation. This

could be due to the fact that the sensor is somewhat protected by the lens, or due to the shorter duration of irradiation compared to other works. That simultaneously would be that the particles interact with these materials and the sensor detects the secondary products from these interactions.

6.2 Proton beam experiment

The main goal of the proton beam experiment is to test the CMOS camera's durability under high-energetic proton particles, as encountered by DISCOSAT-1 in LEO, and characterize its performance as a dosimeter. The second goal is to examine how it responds to different proton energies, aiming to identify any potential energy dependency from the image detections.

6.2.1 Dose measurement

During and after the irradiation experiments, there was no noticeable damage, degradation or saturation in the camera sensor, proving its durability under high energetic protons (up to 244 MeV). The mesh plots in figure 5.15 imply a higher energy position at the higher energy of 244 MeV. As described in detail in section 5.2.3, the measure of dose was investigated through 3 different features: activated pixels, pixel intensity and particle count, which was derived from a processing algorithm described in 5.2.2. The analyses from all these attributes confirmed the proportionality of dose measurement with increase of dose, and by utilizing the linear regression algorithm, a linear equation was derived as shown in 5.2.3.1. The Mean Squared Error (MSE) metric was used for evaluation of the fitted model yielding to a large error. There could be a few reasons behind this result. The data show high variability with MU values that change by the range of the power of 10, and reach 50.000, showing a wide scatter around the regression line. The very limited amount of data points also highly contributes into the model's poor performance. Similarly and dependably to the MU values, the numbers of particle counts are vastly different from the class 1 MU to 50.000 MU and this variability in values can also cause a high MSE. The other important factor to consider is the algorithm's used for the particle count and its performance and reliability. Overall, even through the linear relationship could not be defined precisely, the proportionality is visible throughout the data visualisation analysis and for all 3 features.

Regarding the particle count evaluation, by knowing the flux, the area of the sensor and the FPS used, the total expected protons were estimated for 1MU to be 12.5. The detecting

algorithm, however detected 22 protons for that run, which is almost twice. The reasons for this divergence in these measurements could be multiple. The flux was roughly estimated so the initial measurement could be inaccurate, or just the intensity variation of the beam not been calculated accurately. As mentioned before, due to the high intensity of the proton beam, secondary particles could have also been detected from the sensor, produced by both the materials of the camera in front of the sensor but also the enforcement of the target room. It's also important to mention that due to the lack of documentation for the coral camera's lens and surrounding material, an accurate simulation of the interaction could not been modelled, which could have been beneficial. Another possible explanation for this discrepancy could be that the entire beam spot was not within the sensor area. Conducting a calibration technique against a known dosimeter could also correlate the camera's proton event count with the actual radiation dose, taking into account any efficiencies or sensitivities of the camera sensor to the proton beam. By extension, there was not any other way to evaluate the accuracy of processing algorithm other than a careful visual inspection throughout the processing steps visualised in 5.16. Consequently, it is uncertain which calculation is the most accurate one.

6.2.2 Energy

The analysis in section 5.2.3.2, is dedicated to the investigation of the energy dependency of the camera's sensor activations, through analysis of the experimental data acquired from the proton beam experiment. The first part of this analysis, is based on the activated pixels and pixel intensities against energy. Each data point in these data visualisations represents the energy deposited in the sensor for each run, at different proton energy levels and the same Monitor Units (MU). As seen in figures 5.21 there was no clear proportionality between the energy levels and the pixel activation as one would intuitively expect.

Advanced density visualisation in the figures 5.22 for the particle counts and average particle size derived the processing algorithm, shows a more detailed behaviour of each energy class, with the energies 23-33 MeV behaving similarly but the lower energy of 5.5 MeV showing a higher density. For the class with the higher energy of 244 MeV, the sensor behaves very differently with a flat density, meaning that there is no range of the particle counts. Overall, the particle energy does not seem to create a distinguishable behavioural pattern to the sensor's activation. However, the activation from the class with the higher energy of 244 MeV is significantly different than the ones from rest of the classes, suggesting that there could be threshold

of between 122 and 244 MeV that changes the pattern of pixel activation. This hypotheses would be more data especially on that range in order to calibrate that energy threshold. The time-series plots in figure 5.23 show that change of behaviour as well.

The initial aspiration for this experiment was to gather a labelled dataset for different energies attempting to develop a machine learning classification model to predict the particle energy level for new unseen data. As mentioned in 4.4, there is limited research in energy prediction using particle detections captured by CMOS sensors. Due to the limited data and the data analysis outcome showing no proportionality between activations and proton energies, the particle classification problem according to proton energies was not investigated further in this project.

Another important observation consists of the relatively low numbers of long tracks throughout images captured from all experiments. Even though the data analysis of the tracks from the initial experiments are promising 5.8, considering the unreliable labelled dataset, their gravity could not be verified. However, other works suggest that γ rays produce much longer tracks in detection derived using CMOS sensors [39]. Additionally, during the proton beam experiment, the camera was positioned angled to the pencil beam, and longer tracks were expected to be captured by the camera. However, the amount of longer tracks was roughly similar to the rest of the detection images captured during the experiments with the perpendicular position of the camera. This could be explained by the Coral camera's CMOS architecture Backside Illuminated CMOS (BSI). This architecture offers quick readout speeds not making it ideal for the capture of objects in motion, by extension moving particles.

Chapter 7

Future Work

The main purpose of this project is to characterize the DISCOSAT-1 camera for different proton energies as encountered in LEO. These sections cover the limitations of this project and potential future research work and considerations. In a hypothetical scenario, future work would also involve to get data from the satellite in order to gain real radiation particle images from LEO for further analysis. Comparing real-world data with laboratory results would validate the sensor's response and improve calibration techniques. Future work should focus on significantly increasing the amount of data by repeating experiments under more controlled and thorough experimental setups.

7.0.1 Irradiation experiments

In regards to the irradiation experiments described in section 5.1 and discussed in section 6.1, the most important limitation lies in the lack of reliability of the type of particles detected. The high likelihood of mislabelled data limits the particle classification capabilities greatly. A precisely controlled experimental set up should be conducted in the future by deliberate shielding of particles for each source, to specify the type of particle emitted and detected, in order to leverage this uncertainty. A more accurate labelled dataset would be used for advanced supervised machine learning algorithms for particle classification as the literature review confirms [39]. If repeating the experiments under a more sophisticated set up is not feasible, the data acquired could be used as new unseen data for a machine learning model that has been trained on a more accurately labelled dataset. Since this would require significant resources, and the labelled data would most likely be from a different sensor, the option of labelling through unsupervised clustering could also lead to a classification model but with some considerable uncertainty.

7.0.2 Proton beam experiment

Even if the proportionality of dose measurement and pixel activation has been established, the measurements of particle counts versus the expected counts are not precise. Future experiments would address this in order to evaluate and validate the sensor's response and detection and processing more accurately. Future experiments should aim to refine the accuracy of particle detection and processing. This would involve using more precise dosimeters and simulation tools to better understand the interactions between proton particles and the sensor. Furthermore, collecting data across a wider range of proton energies will help in covering a wider spectrum of proton energies encountered in LEO and investigate in more depth the energy dependency since the lack of data in that spectrum is significant. Each energy level should have an expanded dataset to ensure robust statistical analysis and improved reliability of the results. Investigating the energy point at which the camera's sensor becomes saturated or damaged is of great importance. Discovering the saturation threshold is crucial for defining operational limits and ensuring the camera's durability in space environments. The project's findings highlight the importance of irradiation studies for spacecraft cameras. Camera irradiation calibration is essential for ensuring the reliability and performance of imaging systems in space. The limitations and uncertainties encountered in this project can serve as valuable milestones for future camera characterization efforts within the DISCO project and similar initiatives. Addressing these issues carefully will improve the future set ups and procedures of camera irradiation experiments.

Chapter 8

Conclusion

The research carried out in this study is investigating the capabilities and limitations of DISCOSAT-1 satellite's CMOS camera for the use of cosmic radiation detection through characterization. The collected data from the irradiation experiments conducted, using radiation sources and a proton beam, have contributed to our broader understanding of the camera's response and performance to radiation particles.

The irradiation experiments demonstrated that the CMOS camera successfully detects various types of radiation particles without significant degradation or saturation. This confirms that the camera is well suited and efficient as a particle detector. The camera can effectively be used for measuring the cosmic ray flux and to the sensor through a particle counting algorithm, without affecting its image capturing ability. The features such as pixel intensity and activated pixels carry information on the energy deposited to the sensor by the particles and they have the potential to be used for particle classification. While initial results were promising, overlapping clustering of type of particle classes, possibly due to secondary radiation, made the particle type classification extremely difficult. The results did not support the premise that each source emits a particular type of radiation, highlighting the complexity of the real-world radiation detection and the need for a well considered experimental set up. The data analysis indicated that linear classifiers would not be suitable for this classification problem, and unsupervised learning methods were examined as an alternative solution to the mislabelling issue, albeit with some inherent uncertainties.

The CMOS camera exhibited durability under high-energy proton irradiation, with no noticeable damage to its components up to 244 MeV, verifying its robustness for space missions. There is a significant difference in the energy deposited at 244 MeV nonetheless, indicating a change in the sensor's activation at a point in between 122 and 244 MeV. The proportionality between the dose delivered and the features extracted was confirmed through data analysis, showing that the camera can be used a dose meter, even if the linear regression model used did

not provide a reliable means to quantify this relationship. Moreover, discrepancies in particle count detection indicated potential issues with either the beam's intensity variation, or the possible detection of secondary particle, or the miscounting of the developed algorithm. Analysis of energy dependency revealed no clear proportionality between proton energy levels and pixel activation, suggesting that further research with a wider range of energy levels is necessary to fully understand this dependency.

The findings of this research underline the significant potential of the CMOS camera for space applications, particularly in the context of radiation detection and characterization. The durability and detection capabilities demonstrated in this study are promising, offering a reliable and robust solution for radiation monitoring in harsh space environments. However, the research also highlights critical challenges that need to be addressed to optimize the performance of the camera in detecting and classifying radiation particles. Accurate particle classification remains a complex issue due to overlapping features and potential for secondary radiation. Advanced data analysis techniques and more controlled experimental setups are essential to improve the reliability and accuracy of particle detection. Although the energy dependency analysis using a labeled dataset did not yield significant results, it highlights the importance of irradiation studies for spacecraft cameras. Ensuring the reliability and performance of imaging systems in space, requires thorough camera irradiation calibration. These findings will guide future camera characterization efforts within the DISCO project leading to improved procedures for irradiation experiments.

In conclusion, this thesis underscores the critical importance of irradiation studies for spacecraft cameras. Proper calibration of camera irradiation is essential to ensure the reliability and performance of imaging systems in space. While significant progress has been made, the research highlights important challenges and areas for future exploration. By addressing these challenges through more controlled experiments and advanced data analysis techniques, the reliability and effectiveness of CMOS cameras for radiation detection can be significantly improved, paving the way for their successful deployment in space missions. The insights gained from this study provide a solid foundation for future research and development efforts aimed at enhancing the capabilities of CMOS cameras in radiation environments.

GLOSSARY

BSI Back-Side Illumination. 18

CDF Cumulative Distribution function. 31

CMOS Complementary metal–oxide–semiconductor. 5, 6, 13, 20, 22, 23, 33, 48, 52–54, 56

COTS Commercial off-the-shelf. 22

CREDO Cosmic Ray Extremely Distributed Observatory. 13

CSI Camera Serial Interface. 37

DISCO Danish Student CubeSat Program. 10, 58, 60

ESA Extensive Air Showers. 14

FPS Frames Per Second. 38, 54

GCR Galactic Cosmic Ray. 14, 15

GMM Gaussian Mixture Model. 34, 35, 53

IPU Image Processing Unit. 7, 13, 25

ISP Image Signal Processor. 17

KDE Kernel Density Estimation. 48

LEO Low Earth Orbit. 6, 8, 13, 14, 57, 58

LET Linear Energy Transfer. 12

MSE Mean Squared Error. 46, 47, 54

MU Monitor Unit. 38, 44, 45, 54

PBS Pencil beam scanning. 36

PCA Principal Component Analysis. 32, 33, 35, 53

PCR Primary Cosmic Ray. 11

SEP Solar Energetic Particles. 14

SEU Single Event Upset. 12, 21

SPENVIS Space Environment Information System. 14, 15

TPU Tensor Processing Unit. 8, 13

LIST OF REFERENCES

- [1] Space technology. [Online]. Available: <https://www.csensor.com/technology-space>
- [2] H. G. Kang, J.-J. Song, K. Lee, K. C. Nam, S. J. Hong, and H. C. Kim, “An investigation of medical radiation detection using CMOS image sensors in smartphones,” vol. 823, pp. 126–134. [Online]. Available: <https://linkinghub.elsevier.com/retrieve/pii/S016890021630167X>
- [3] Ieva. CubeSat 101: The comprehensive guide to understanding satellite technology - NanoAvionics. [Online]. Available: <https://nanoavionics.com/blog/cubesat-101-the-comprehensive-guide-to-understanding-satellite-technology/>
- [4] B. M. M. Bomani, “CubeSat technology past and present: Current state-of-the-art survey,” *National Aeronautics and Space Administration*. [Online]. Available: <https://ntrs.nasa.gov/api/citations/20210000201/downloads/TP-20210000201.pdf>
- [5] V. Lalucaa, E. Berdin, F. Larnaudie, J.-M. Belloir, C. Codreanu, and L. Chavanne, “Evaluation of microlenses, color filters, and polarizing filters in cis for space applications,” *Sensors*, vol. 23, no. 13, p. 5884, 2023. [Online]. Available: <https://www.mdpi.com/1424-8220/23/13/5884>
- [6] S. Y. Christina Gaitanou, David Nikolaj Vinje, “Cubesat camera control for disco-1 research project,” 8 2023, unpublished research project.
- [7] A. L. M. Dimitra Atri, “Cosmic Rays and Terrestrial Life: A Brief Review,” *Astroparticle Physics*, vol. 53, pp. 186–190, 1 2014. [Online]. Available: <https://arxiv.org/abs/1211.3962>
- [8] R. A. Mewaldt, “Cosmic rays,” *Macmillian Encyclopedia of Physics*, vol. 57, 1996. [Online]. Available: https://sites.srl.caltech.edu/~rmewaldt/cos_encyc.html
- [9] L. J. Herrera, C. J. Todero Peixoto, O. Baños, J. M. Carceller, F. Carrillo, and A. Guillén, “Composition classification of ultra-high energy cosmic rays,” vol. 22, no. 9, p. 998. [Online]. Available: <https://www.mdpi.com/1099-4300/22/9/998>
- [10] N. Aeronautics and S. Administration, “Cosmic rays,” 2017, last accessed 30 May 2024. [Online]. Available: https://imagine.gsfc.nasa.gov/science/toolbox/cosmic_rays1.html
- [11] E. Fermi, “On the origin of the cosmic radiation,” *Physical Review*, vol. 75, no. 8, p. 1169, 1949. [Online]. Available: <https://doi.org/10.1103/PhysRev.75.1169>
- [12] L. O. Drury, “Origin of Cosmic Rays,” *Astroparticle Physics*, p. 15, 3 2012. [Online]. Available: <https://arxiv.org/abs/1203.3681>

- [13] Z. Szadkowski, “Introductory chapter: Ultrahigh-energy cosmic rays,” in *Cosmic Rays*, Z. Szadkowski, Ed. InTech. [Online]. Available: <http://www.intechopen.com/books/cosmic-rays/introductory-chapter-ultrahigh-energy-cosmic-rays>
- [14] M. Boezio, R. Munini, and P. Picozza, “Cosmic ray detection in space,” vol. 112, p. 103765. [Online]. Available: <https://linkinghub.elsevier.com/retrieve/pii/S0146641020300120>
- [15] K. LaBel, “Radiation effects on electronics 101.”
- [16] The may 2024 solar storm: your questions answered. [Online]. Available: https://www.esa.int/Space_Safety/Space_weather/The_May_2024_solar_storm_your_questions_answered
- [17] Solar cycle 25 is here. NASA, NOAA scientists explain what that means - NASA. [Online]. Available: <https://www.nasa.gov/news-release/solar-cycle-25-is-here-nasa-noaa-scientists-explain-what-that-means/>
- [18] R. A. MacDougall. Cosmic radiation detection takes front seat during NASA’s artemis i space mission. [Online]. Available: <https://www.nibib.nih.gov/news-events/newsroom/cosmic-radiation-detection-takes-front-seat-during-nasa%E2%80%99s-artemis-i-space-mission>
- [19] Observatorio pierre auger. [Online]. Available: <https://www.auger.org/>
- [20] Alpha magnetic spectrometer - NASA. [Online]. Available: <https://www.nasa.gov/alpha-magnetic-spectrometer/>
- [21] O. Sushchov, P. Homola, N. Dhital, Bratek, P. Poznański, T. Wibig, J. Zamora-Saa, K. A. Cheminant, D. A. Castillo, D. Góra, P. Jagoda, J. Jałocha, J. F. Jarvis, M. Kasztelan, K. Kopański, M. Krupiński, M. Michałek, V. Nazari, K. Smelcerz, K. Smolek, J. Stasielak, and M. Sułek, “Cosmic-ray extremely distributed observatory: a global cosmic ray detection framework,” vol. 7, no. 1, pp. 23–29. [Online]. Available: <http://arxiv.org/abs/1709.05230>
- [22] P. Homola, D. E. A. Castillo, D. Góra, A. R. Duffy, B. Hnatyk, P. Jagoda, M. Kasztelan, K. Kopański, P. Kovacs, M. Krupiński, A. Mozgova, V. Nazari, M. Niedźwiecki, W. Noga, D. Ostrogórski, K. Smolek, J. Stasielak, O. Sushchov, T. Wibig, K. W. Woźniak, and J. Zamora-Saa, “Public engagement as a scientific tool to implement multi-messenger strategies with the cosmic-ray extremely distributed observatory.” [Online]. Available: <http://arxiv.org/abs/1908.09734>
- [23] W. Suparta and S. K. Zulkeple, “Spatial analysis of galactic cosmic ray particles in low earth orbit/near equator orbit using SPENVIS,” vol. 495, p. 012040. [Online]. Available: <https://iopscience.iop.org/article/10.1088/1742-6596/495/1/012040>
- [24] S. Gohl, B. Bergmann, H. Evans, P. Nieminen, A. Owens, and S. Posipsil, “Study of the radiation fields in LEO with the space application of timepix radiation monitor (SATRAM),” vol. 63, no. 5, pp. 1646–1660. [Online]. Available: <https://linkinghub.elsevier.com/retrieve/pii/S0273117718308706>

- [25] O. Adriani, G. C. Barbarino, G. A. Bazilevskaya, R. Bellotti, M. Boezio, E. A. Bogomolov, M. Bongi, V. Bonvicini, S. Bottai, A. Bruno, F. Cafagna, D. Campana, R. Carbone, P. Carlson, M. Casolino, G. Castellini, I. A. Danilchenko, C. De Donato, C. De Santis, N. De Simone, V. Di Felice, V. Formato, A. M. Galper, A. V. Kareljin, S. V. Koldashov, S. Koldobskiy, S. Y. Krutkov, A. N. Kvashnin, A. Leonov, V. Malakhov, L. Marcelli, M. Martucci, A. G. Mayorov, W. Menn, M. Mergé, V. V. Mikhailov, E. Mocchiutti, A. Monaco, N. Mori, R. Munini, G. Osteria, F. Palma, B. Panico, P. Papini, M. Pearce, P. Picozza, M. Ricci, S. B. Ricciarini, R. Sarkar, V. Scotti, M. Simon, R. Sparvoli, P. Spillantini, Y. I. Stozhkov, A. Vacchi, E. Vannuccini, G. I. Vasilyev, S. A. Voronov, Y. T. Yurkin, G. Zampa, N. Zampa, and V. G. Zverev, “Trapped proton fluxes at low earth orbits measured by the PAMELA experiment,” vol. 799, no. 1, p. L4. [Online]. Available: <http://arxiv.org/abs/1412.1258>
- [26] C. Granja, S. Polansky, Z. Vykydal, S. Pospisil, A. Owens, Z. Kozacek, K. Mellab, and M. Simcak, “The SATRAM timepix spacecraft payload in open space on board the probav satellite for wide range radiation monitoring in LEO orbit,” vol. 125, pp. 114–129. [Online]. Available: <https://linkinghub.elsevier.com/retrieve/pii/S0032063316300216>
- [27] European Space Agency, “SPENVIS - Space Environment Information System,” 2024, accessed: 2024-06-12. [Online]. Available: <https://www.spenvis.oma.be>
- [28] Solar cycle progression | NOAA / NWS space weather prediction center. [Online]. Available: <https://www.swpc.noaa.gov/products/solar-cycle-progression>
- [29] Solar cycle 25 is here. NASA, NOAA scientists explain what that means - NASA. [Online]. Available: <https://www.nasa.gov/news-release/solar-cycle-25-is-here-nasa-noaa-scientists-explain-what-that-means/>
- [30] X. Shoulong, Z. Shuliang, and H. Youjun, “\$\\gamma\$ -ray detection using commercial off-the-shelf CMOS and CCD image sensors,” vol. 17, no. 20, pp. 6599–6604. [Online]. Available: <http://ieeexplore.ieee.org/document/7994685/>
- [31] S. Lin, S. Ning, H. Zhu, T. Zhou, C. L. Morris, S. Clayton, M. J. Cherukara, R. T. Chen, and Z. Wang, “Neural network methods for radiation detectors and imaging,” vol. 12, p. 1334298. [Online]. Available: <https://www.frontiersin.org/articles/10.3389/fphy.2024.1334298/full>
- [32] What’s the difference between CMOS, BSI CMOS, and stacked CMOS? Section: Cameras. [Online]. Available: <https://au.pc当地.com/cameras-1/94932/whats-the-difference-between-cmos-bsi-cmos-and-stacked-cmos>
- [33] “Camera datasheet.”
- [34] M. Perez, M. S. Haro, I. Sidelnik, L. Tozzi, D. R. Brito, C. Mora, J. J. Blostein, M. G. Berisso, and J. Lipovetzky, “Commercial CMOS pixel array for beta and gamma radiation particle counting,” in *2015 Argentine School of Micro-Nanoelectronics, Technology and Applications (EAMTA)*. IEEE, pp. 11–16. [Online]. Available: <http://ieeexplore.ieee.org/document/7237371/>
- [35] *Ionizing Radiation*. John Wiley Sons, Ltd, 1986, ch. 1, pp. 1–19. [Online]. Available: <https://onlinelibrary.wiley.com/doi/abs/10.1002/9783527617135.ch1>

- [36] B. R. Martin, *Nuclear and Particle Physics: An Introduction*. Chichester, UK: John Wiley & Sons, 2006.
- [37] X-rays. [Online]. Available: <https://www.nibib.nih.gov/science-education/science-topics/x-rays>
- [38] *Charged-Particle Interactions in Matter*. John Wiley Sons, Ltd, 1986, ch. 8, pp. 160–202. [Online]. Available: <https://onlinelibrary.wiley.com/doi/abs/10.1002/9783527617135.ch8>
- [39] M. Pérez, J. Lipovetzky, M. Sofo Haro, I. Sidelnik, J. J. Blostein, F. Alcalde Bessia, and M. G. Berisso, “Particle detection and classification using commercial off the shelf CMOS image sensors,” vol. 827, pp. 171–180. [Online]. Available: <https://linkinghub.elsevier.com/retrieve/pii/S0168900216302844>
- [40] S. Xu, S. Zou, Y. Han, T. Zhang, and Y. Qu, “Obtaining high-dose-rate γ -ray detection with commercial off-the-shelf CMOS pixel sensor module,” vol. 19, no. 16, pp. 6729–6735. [Online]. Available: <https://ieeexplore.ieee.org/document/8694826/>
- [41] Q.-Q. Cheng, Y.-Z. Yuan, C.-W. Ma, and F. Wang, “Gamma measurement based on CMOS sensor and ARM microcontroller,” vol. 28, no. 9, p. 122. [Online]. Available: <http://link.springer.com/10.1007/s41365-017-0276-x>
- [42] J. Florczak, T. Neubert, E. Zimmermann, H. Rongen, M. Kaufmann, I. Rienäcker, W. Hajdas, M. Riese, and S. Van Waasen, “Calibration of the deposited energy in CMOS imagers for particle detection on nanosatellites,” vol. 70, no. 8, pp. 1966–1972. [Online]. Available: <https://ieeexplore.ieee.org/document/10122703/>
- [43] L. J. Herrera, C. J. Todero Peixoto, O. Baños, J. M. Carceller, F. Carrillo, and A. Guillén, “Composition classification of ultra-high energy cosmic rays,” vol. 22, no. 9, p. 998. [Online]. Available: <https://www.mdpi.com/1099-4300/22/9/998>
- [44] V. Palani, T. Thanarajan, A. Krishnamurthy, and S. Rajendran, “Deep learning based compression with classification model on CMOS image sensors,” vol. 40, no. 3, pp. 1163–1170. [Online]. Available: <https://ieta.org/journals/ts/paper/10.18280/ts.400332>
- [45] M. Niedzwiecki, K. Rzecki, M. Marek, P. Homola, K. Smelcerz, D. A. Castillo, K. Smolek, B. Hnatyk, J. Zamora-Saa, A. Mozgová, V. Nazaric, D. Gora, K. Kopanski, T. Wibig, A. R. Duffy, J. Stasielak, Z. Zimboras, and M. Kasztelan, “Recognition and classification of the cosmic-ray events in images captured by CMOS/CCD cameras.” [Online]. Available: <http://arxiv.org/abs/1909.01929>
- [46] Z. Peng, Y. Fu, Y. Wei, Y. Zuo, S. Niu, J. Zhu, Y. Guo, F. Liu, P. Li, C. He, and Y. Li, “Investigation of proton single-event transient in CMOS image sensor,” vol. 14, no. 1, p. 015211. [Online]. Available: <https://doi.org/10.1063/5.0184659>
- [47] J. Florczak, T. Neubert, K. El Maghawry, E. Zimmermann, H. Rongen, M. Kaufmann, F. Olszewski, and S. Van Waasen, “Radiation monitor extension for CMOS imaging instruments in nanosatellites,” vol. 69, no. 7, pp. 1651–1658. [Online]. Available: <https://ieeexplore.ieee.org/document/9686712/>

- [48] P. Kovář, P. Puričer, E. Benton, and J. Mikeš, “Demonstration of the capability of 1u CubeSat for measurement of the energy spectrum on LEO,” vol. 11, no. 20, p. 3390. [Online]. Available: <https://www.mdpi.com/2079-9292/11/20/3390>
- [49] BISMUTH-207. [Online]. Available: <https://www.cyclotronzao.ru/en/products/radiochemicals/vismut-207.php>
- [50] D. E. Alburger and A. W. Sunyar, “Decay of Bi^{207} ,” vol. 99, no. 3, pp. 695–702, publisher: American Physical Society. [Online]. Available: <https://link.aps.org/doi/10.1103/PhysRev.99.695>
- [51] (2019) Interpretation of bi-207 decay spectrum. [Online]. Available: <https://www.physicsforums.com/threads/interpretation-of-bi-207-decay-spectrum.976312/>
- [52] “Uranium-238,” page Version ID: 1227532684. [Online]. Available: <https://en.wikipedia.org/w/index.php?title=Uranium-238&oldid=1227532684>
- [53] OpenStax, “31.4 nuclear decay and conservation laws,” book Title: College Physics. [Online]. Available: <https://pressbooks.uiowa.edu/clonedbook/chapter/nuclear-decay-and-conservation-laws/>
- [54] uranium. [Online]. Available: <https://pubs.usgs.gov/of/2004/1050/uranium.htm>
- [55] O. US EPA. Radioactive decay. [Online]. Available: <https://www.epa.gov/radiation/radioactive-decay>
- [56] Radioactive decay | chemistry: Atoms first. [Online]. Available: <https://courses.lumenlearning.com/suny-chem-atoms-first/chapter/radioactive-decay-2/>
- [57] Cobalt 60. [Online]. Available: <https://www.slideshare.net/slideshow/cobalt-60/43168040>
- [58] M. Saro, V. Kršjak, M. Petriska, and V. Slugeň, “Sodium-22 source contribution determination in positron annihilation measurements using GEANT4,” p. 020039. [Online]. Available: <https://pubs.aip.org/aip/acp/article/700205>
- [59] “Recommended nuclear decay data,” 2010. [Online]. Available: https://www.ezag.com/fileadmin/ezag/user-uploads/isotopes/isotopes/Isotrak/isotrak-pdf/Decay_Schema_Data/Na-22.pdf
- [60] S. V. Poluianov, G. A. Kovaltsov, A. L. Mishev, and I. G. Usoskin, “Production of cosmogenic isotopes ^7Be , ^{10}Be , ^{14}C , ^{22}Na , and ^{36}Cl in the atmosphere: Altitudinal profiles of yield functions,” vol. 121, no. 13, pp. 8125–8136. [Online]. Available: <https://agupubs.onlinelibrary.wiley.com/doi/10.1002/2016JD025034>
- [61] A. Grianti. Principal component analysis. [Online]. Available: <https://towardsdatascience.com/principal-component-analysis-3c39fbf5cb9d>
- [62] “Recommended nuclear decay data (u-238),” 2010. [Online]. Available: https://www.ezag.com/fileadmin/ezag/user-uploads/isotopes/isotopes/Isotrak/isotrak-pdf/Decay_Schema_Data/U-238.pdf

- [63] Table of isotopes decay data. [Online]. Available: <http://nucleardata.nuclear.lu.se/toi/nuclide.asp?iZA=920238&sortG=I&sortA=E>
- [64] 2.1. gaussian mixture models. [Online]. Available: <https://scikit-learn/stable/modules/mixture.html>
- [65] R. Ravihara. Gaussian mixture model clearly explained. [Online]. Available: <https://towardsdatascience.com/gaussian-mixture-model-clearly-explained-115010f7d4cf>
- [66] Research facilities - aarhus universitetshospital. [Online]. Available: <https://www.en.auh.dk/departments/the-danish-centre-for-particle-therapy/research/research-facilities/>
- [67] A. Darafsheh, Y. Hao, X. Zhao *et al.*, “Spread-out bragg peak proton flash irradiation using a clinical synchrocyclotron: proof of concept and ion chamber characterization,” *Med Phys*, vol. 48, pp. 4472–4484, 2021.
- [68] H. Liu and J. Y. Chang, “Proton therapy in clinical practice,” vol. 30, no. 5, pp. 315–326. [Online]. Available: <https://www.ncbi.nlm.nih.gov/pmc/articles/PMC4013396/>
- [69] nathancy. Answer to ”particle detection with python OpenCV”. [Online]. Available: <https://stackoverflow.com/a/72120738>
- [70] P. Sharma. Introduction to k-means clustering algorithm. [Online]. Available: <https://www.analyticsvidhya.com/blog/2019/08/comprehensive-guide-k-means-clustering/>
- [71] V. A. D. K-means clustering algorithm from scratch. [Online]. Available: <https://www.machinelearningplus.com/predictive-modeling/k-means-clustering/>
- [72] C. Levraud, “Quantization/clustering: when and why does k-means work?” [Online]. Available: <http://arxiv.org/abs/1801.03742>
- [73] J. Frost. Mean squared error (MSE). [Online]. Available: <https://statisticsbyjim.com/regression/mean-squared-error-mse/>